The 2017 Kos Sequence: Aftershocks Relocation and Coseismic Rupture Process Constrained from Joint Inversion of Seismological and Geodetic Observations

Vasileios Karakostas[1], Maya Ilieva[2], Anastasios Kostoglou[1], Damian Tondaś[2], Eleftheria Papadimitriou[1], Maria Mesimeri[3], and Begum Koca[4]

[1]Geophysics Department, Aristotle University of Thessaloniki, GR54124 Thessaloniki, Greece

[2]Institute of Geodesy and Geoinformatics, Wroclaw University of Environmental Life and Sciences, 50–357 Wroclaw, Poland

[3]Department of Earth Sciences, ETH, Zurich, Switzerland

[4]Department of Geophysical Engineering, Faculty of Engineering, Ankara University

Corresponding author: Vasileios Karakostas (vkarak@geo.auth.gr)

Key Points:

- The 2017 Kos M_w6.6 main shock and its aftershock sequence revealed the geometric and kinematic properties of a major north dipping normal fault
- Rupture process and coseismic slip model in agreement with aftershock distribution define the seismogenic layer and imply nucleation at its lower part
- Coulomb stress changes evidence the main shock possible triggering by recent moderate earthquakes, and aftershock activity triggering due to the coseismic slip

Abstract

On 20 July 2017 an M_w6.6 earthquake occurred offshore Kos Island, the largest to occur in the affected area in the instrumental era, and in the past 60 years in southeastern Aegean Sea. We estimated the aftershocks relative locations by applying the double difference technique using both differential times from phase picked data and waveform cross correlation. The relocated aftershocks are clustered at least in three distinctive patches, creating a zone getting a total length of about 40 km, elongated in a nearly east–west direction, mainly concentrated at depths 8–15 km, with the main shock hypocenter placed at ~13 km, implying a seismogenic layer of 7 km thickness, indicative for normal faulting earthquakes with M_{max}~6.5. The aftershock fault plane solutions are predominantly suggestive of normal faulting in response to the north south extension of the back arc Aegean area. We further applied the satellite radar interferometry (InSAR) technique to define the coseismic surface displacements. This field of deformation along with the available vectors of displacement measured by Global Navigation Satellite System (GNSS) technique were combined with the seismological data to determine the rupture geometry and process, with the coseismic slip ranging between 0.5 and 2.3 m. The peak moment release occurred in the depth interval of 9–11 km, consistent with the depth distribution of seismicity in the study area. We used the variable slip model to calculate Coulomb stress changes and investigate possible triggering due to stress transfer to the nearby fault segments.

Plain Language Summary

The 21 July2017 M_w6.6 Kos, Greece, earthquake ruptured a normal fault in the back arc Aegean area. The area was not visited recently by strong earthquakes, and the main rupture along with the vigorous aftershock sequence, constitute a challenge in investigating source and deformation properties, with implications to regional seismotectonics. We relocated aftershock seismicity and with the highly relocated hypocenters, we defined the main rupture geometry, a 32 km long north-dipping fault, and identified secondary activated fault segments of the local fault network, the activation of which is well-explained by stress transfer due to the main shock coseismic slip. We applied satellite radar interferometry (InSAR) technique to define the coseismic surface displacements. We combined Global Navigation Satellite System (GNSS) with the seismological data to determine the fault

geometry and study the rupture process. Our findings document the north dipping fault plane and provide a comprehensive image of the characteristics of the seismic sequence and the associated local fault network.

1 Introduction

On 20 July 2017, at 22:31:10 UTC (01:31 local time), a moment magnitude M_w6.6 earthquake occurred close to the northeastern coastline of Kos Island and Aegean coast of Turkey (Fig. 1, yellow rectangle). Its occurrence seriously affected the city of Kos and several minor towns in Turkey mainland to the northeast of the epicentral area. Southeastern Aegean Sea is one of the most seismically active areas in the Eastern Mediterranean, with a distinctive seismic zone extending from western Turkey, and characterized mainly by normal faulting and diffuse crustal seismicity. Frequent strong (M>6.0) main shocks are known from historical information and instrumental recordings in this extensional zone, displaying clustering behavior (Papadimitriou et al., 2005). The largest event occurred in 1956 with M_w7.5 (hereafter, we drop the subscript w and refer to the earthquake magnitude as the moment magnitude, unless otherwise noted), associated with a normal fault bounding the southern coastline of the Amorgos Island. Strong events commonly involve shallow normal faulting and occasional have significant strike slip component (Papazachos et al., 1998). Their aftershock sequences settled in characteristic parallel grabens that are formed and bounded by normal faulting both onshore and offshore. The individual slip rates are estimated to be comparatively low ranging between 1-3 mm/yr from geodetic studies (McClusky et al., 2000; Reilinger et al., 2010). Despite the generally slow tectonic loading on the regional fault networks, the strong (M>6.0) earthquake activity is appreciable, associated with the fault segments bounding the flanks of the onshore grabens and the coastlines of the Aegean Islands. The closest main shock of this order of magnitude occurred in 1933 with M=6.6 offshore the southern coastline of the Kos Island.

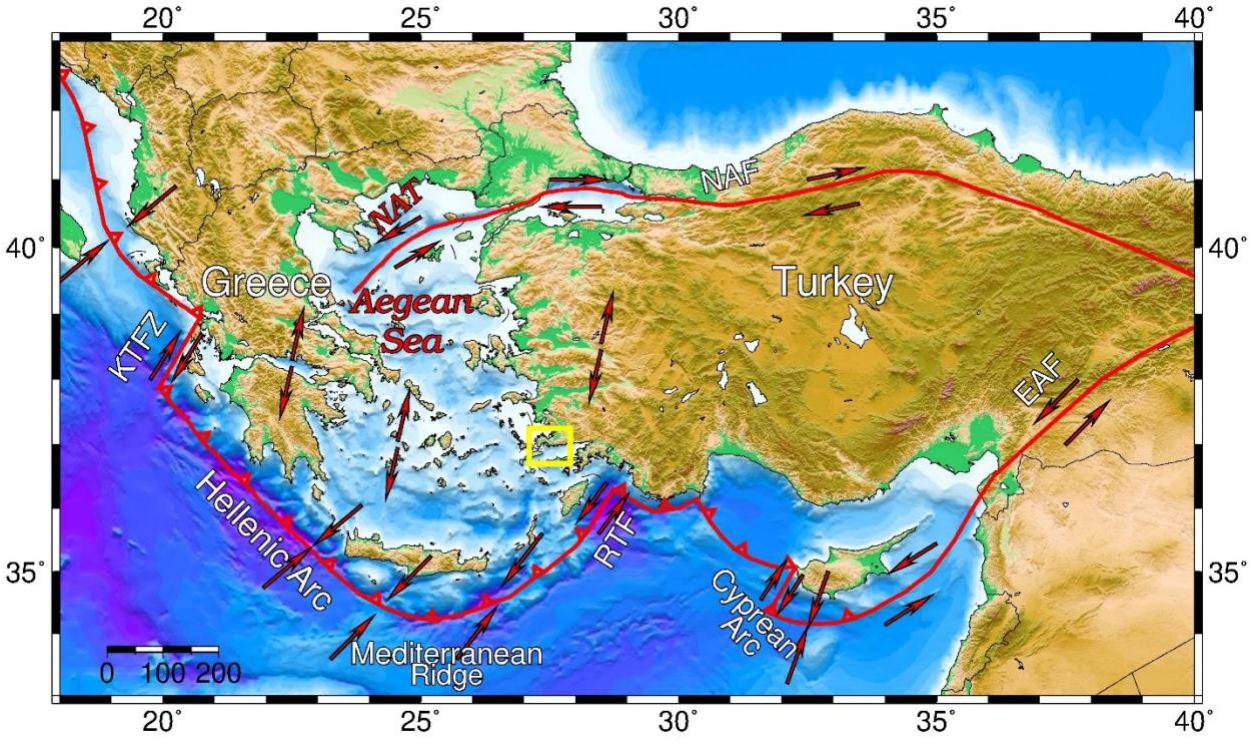

Figure 1. Map of the eastern Mediterranean region along with its major seismotectonic characteristics. The solid red lines represent the active tectonic boundaries, and the arrows represent the direction of the plate relative motion. The yellow square is the study area. NAT, North Aegean Trough; KTFZ, Kefalonia Transform Fault Zone; RTF, Rodos Transform Fault; NAF, North Anatolia Fault; EAF, East Anatolia Fault.

The 2017 Kos main shock is the largest to have occurred in the southeastern Aegean area since 1969 and followed by a rich aftershock sequence, which occupied an area of relative quiescence in the last twenty years. This seismic sequence attracted the attention of several research teams (Table S1) because of the relatively large magnitude of the main shock resulted to the loss of life in both countries, Greece and Turkey, the appreciable aftershock productivity and the accompanying consequences. The global centroid moment tensor (GCMT) solution (https://www.globalcmt.org/CMTcite.html) denotes that the main shock is associated with normal faulting (strike=278°; dip=36°; rake=-82°) with a seismic moment of M_o=1.16×10^{26} dyn•cm, at a centroid depth of 12 km. Four aftershocks attained magnitudes M>5.0, three of them occurring within 15 km of the main shock epicenter and two of those three within the first 24 hours after the main shock. A moderate tsunami was recorded, with a runup of 1.9 m, which Heidarzadeh et al. (2017) attributed to a fault with

length of 25 km, width of 15 km and uniform slip of 0.4 m, independently of the preference for the dip of the fault plane, either to the north or south. A south dipping fault at ~50° was considered by Kiratzi & Koskosidi (2017) and a slip model with bilateral rupture propagation at a rate of 2.8km/s and a maximum value of ~1.6m was proposed, with two shallow slip patches located either side of the hypocenter. Based on the relocated aftershock activity Karakostas et al. (2018) supported a north dipping fault plane. Ocakoğlu et al. (2018) considered the area to be dominated by normal faulting and considerable strike-slip motion according to multichannel seismic profiles.

Tiryakioğlu et al. (2018) analyzed pre- and post-earthquake continuous static Global Navigation Satellite System (GNSS) measurements for defining the coseismic slip distribution, by fitting a southward dipping to ~65 km long fault onto which three patches were constrained with maximum slips of 13, 26 and 5 cm, respectively. In Karasözen et al. (2018) the GNSS measurements performed by Tiryakioglu et al. (2018) were jointly analysed with the deformation patterns received from differential interferograms applying the satellite Interferometry with Synthetic Aperture Radar (InSAR) approach in order to model the geometry of the main rupture. The authors propose a different solution for north direction of the dip of ~37°, with the earthquake nucleation at 11 km and a bilateral and upwards rupture propagation. The aftershock locations defined in the same study reached a depth of 15 km and distribution around the western, eastern and downdip edges of a 25-km long rupture plane. Ganas et al. (2019) applied similar approach to modeled the main fault from joint inversion of deformation field (based on delineated interferometric fringes) derived from InSAR data and co-seismic displacement vectors calculated for stations from several regional networks measured by GNSS. The authors assume a homogeneous slip on a rectangular fault. The result of this study showed the better fitting model of the join inversion for a north-dipping normal faulting case mainly with a significant strike-slip component of 2.03 m, 14 km length and 12.5 km width of the modelled rupture. Similar study (Konca et al., 2019) that also include campaigned GNSS measurements propose a fault model with ~40o, north-dipping, 20-25 km long, E-W striking, normal fault geometry, with coseismic slip exceeding 2 m.

Sboras et al. (2020) used seismological and geological observations to conclude that the main shock and its aftershock sequence evidence the prevailing tectonic setting of the area, consisting of roughly E-W striking normal faults forming inner horsts and grabens. Cordrie et al. (2021) use the fault model proposed by Ganas et al. (2019) to perform tsunami simulations to constrain the source. The authors concluded that the comparison between the maximum wave heights model and the field data favor the north-dipping fault scenario.

The presented results of the most notable published studies on the 2017 Kos event revealed a significant uncertainty in the faulting geometry mainly concerning the dipping direction, and type and size of the slip component. In the present paper, we attempt to clarify processes associated with the 2017 Kos sequence using an abundant data set, comprising seismological and geodetic measurements, and implement them in an integrated inversion fault model. Our study is focused on the coseismic processes but also verifies pre- and postseismic phases of the fault activation (Fig. 2). Our aim is to contribute with a more precise identification of the main rupture and the aftershock sequence properties. The accurately located sequences provide the opportunity to investigate the tectonics and earthquake source properties within a seismically active region, which however was not visited by strong (M>6.0) earthquakes in the last few decades when the regional networks were significantly improved. The 2017 Kos sequence is a significant challenge for this scope, with fault modelling of a major regional fault, and contributes shedding more light to its geometry and kinematic properties, along with the investigation of off fault aftershock activity. Faults that are associated with the numerous aftershocks revealed the characteristics of a local fault network with hierarchical features, where the main rupture possesses the first order.

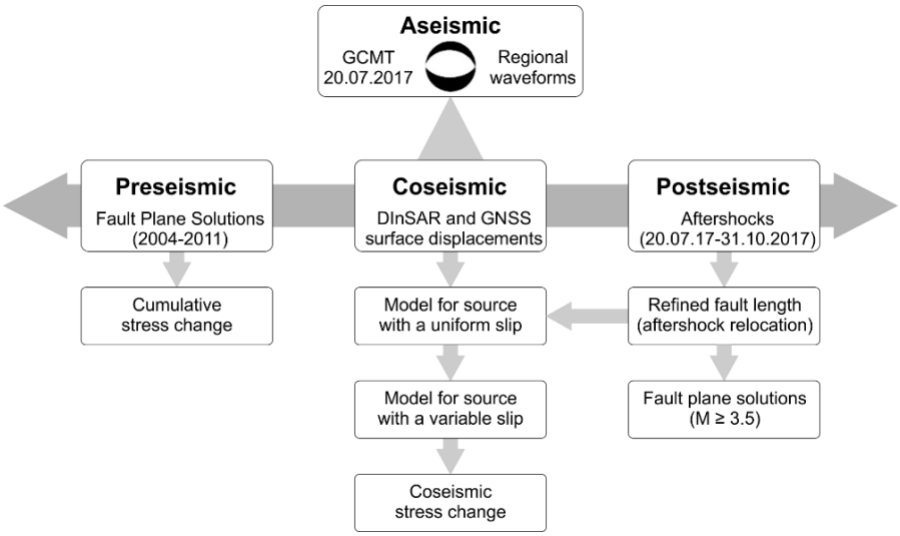

Figure 2. Data and techniques applied in the current research to study the evolution of the rupture and seismic activity related with the 2017 event

The causative fault cannot be unambiguously related with previous known strong (M>6.0) earthquake, since the distinction between the failure of antithetic faults is debatable even for the current main shock, given that in a seismic excitation multiple segments are activated, and the aftershock locations are ambiguously associated to a certain segment among them. The investigation of the 2017 strong seismic activity including the main shock and the refined locations of the subsequent series of aftershocks contributes to the better constraint of the main rupture geometry along with the activated adjacent fault segments, the extension of the seismogenic layer and the seismic sequence evolution. In turn, these findings contribute to the realistic seismic hazard scenario and assessment. Our results reveal that unidentified minor fault segments, either along strike or antithetic to major ones, are adequate to accommodate regional strain capable to culminate in significant seismic activity. Geodetic data obtained by GNSS measurements (Ganas et al., 2019) at ground stations and deformation maps generated by the usage of Differential InSAR (DInSAR) technique applied to two pairs of Sentinel-1 satellite data acquired by the European Space Agency (ESA) are exploited to better identify the fault geometry and calculate a variable

coseismic slip distribution model. This allows for a thorough investigation of stress transfer and determination of possibly triggered secondary fault segments of the local fault network.

2 Seismotectonic setting and past seismicity

The affected area, including Kos Island and Bodrum peninsula, is located in the SE Aegean Sea where an extensive mostly E-W-trending fault population produces remarkable seismicity and frequent strong earthquakes with M6-M7, as the result of relatively fast N-S back arc extension. The area of interest belongs to Gokova basin, filled in with the latest Miocene-Pliocene-Quaternary sediments of maximum thickness ~2.5 km (Kurt et al., 1999). The gulf opened by the north-dipping, mainly E-W-trending Datca fault, which is located at the southern part of the gulf, with antithetic faults at the north, and an overall constant extension rate of at least 1.1 mm/yr. The gulf opening started in late Miocene-Pliocene and the continuing extension might be responsible for a second phase of faulting with WNW-ESE oriented subgrabens in the gulf and major E-W normal faulting in the northeast margin (Kurt et al., 1999). Thus, although the main orientation of the gulf is E-W, the more recent WNW-ESE structures are remarkable in the mid-gulf and in its eastern part. Younger active faulting in the central part, with a NE strike, exhibits sinistral strike-slip motion and acts as a transfer fault (Uluğ et al, 2005).

Tur et al. (2015) consider the orientations of the three families of faults, with NW-SE, E-W and ENE-WSW strikes, as inconsistent with a simple N-S extensional regime. These authors, based on seismic reflection profiles, multibeam bathymetry and GNSS vectors suggested that the area developed as a lazy-S-shaped graben, due to a counterclockwise rotation of the back arc Aegean, as subduction roll back took place during Pliocene-Quaternary. This is the youngest of a series of back arc basins, which started opening from the west during the Pliocene and progressing eastward during the Quaternary.

The SE Aegean area accommodates frequent strong (M>6.0) earthquakes, for which adequate testimonies exist since the 6th century BC (full historical catalog from Papazachos & Papazachou, 2003), given that in the area many significant ancient Greek cities were flourished with developed civilization and scientific observations. The map of Figure 3a depicts the epicenters of the historical (grey stars) and instrumentally recorded (red stars)

earthquakes. The highly clustered historical activity may be attributed to the historical descriptions, which are mainly based on the earthquake damage caused to the important at that time cities. Nevertheless, the severity and frequency of the seismic activity is obvious.

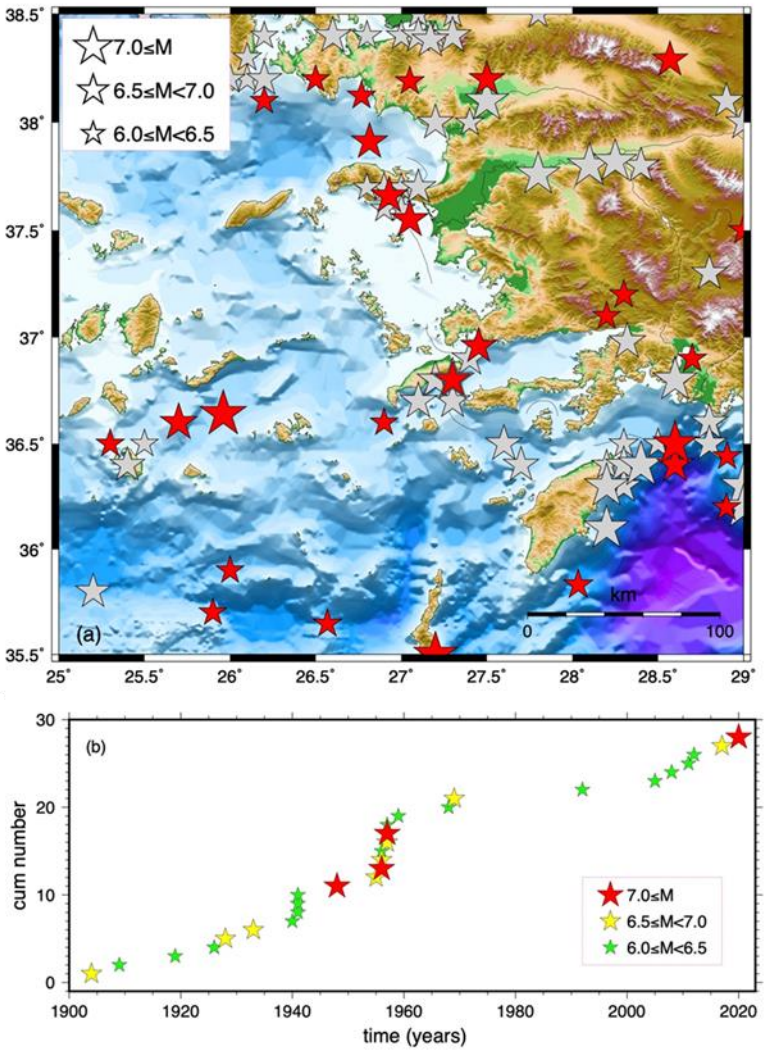

Figure 3. (a) Epicenters of all known strong (M>6.0) historical (grey stars) and instrumental (red stars) earthquakes since 6th century BC that occurred in the southeastern Aegean area (yellow rectangle from Fig.1). The size of the symbols is scaled according to the earthquake magnitude. **(b)** Rate of M>6.0 earthquakes during 20th century. The color and the size of each symbol denote different magnitude ranges, as it is shown in the legend.

Since the beginning of the instrumental era, when the catalog is found complete for M>6.0 earthquakes in the area of Greece, their occurrence rate approximates a value of $\dot{r}$~0.25.

Figure 3b shows the occurrence rate of M>6.0 earthquakes since the beginning of the 20th century, with the activity not equally distributed in time, but with periods of relative quiescence to be alternated with periods of higher activity. It is noteworthy, however, that the activity was intense during the first six decades of the 20th century. A period of remarkable excitation with seven M>6.0 earthquakes in three years, namely 1956-1959, was followed by a period of quiescence after 1970 up to 2005. Even if we will take into account the magnitude estimations uncertainties in the early period of the instrumental catalog, the pattern remains unaltered, and must not be ignored in the estimates of seismic hazard. After 1970 the activity becomes significantly weakened, with a few M>6.0 earthquakes and lack of M>6.5 ones. In the close vicinity of the 2017 main shock, the last M>6.0 earthquake occurred in 1968 near the southwester coast of Kos Island.

Investigation of earthquake mechanisms for moderate earthquakes (Mw>5.0, during 1986-2005) revealed E-W striking high-angle normal faults with small strike slip components occasionally, and the maximum extension axes oriented from N-S to NW-SE (Yolsal-Çevikbilen et al., 2014). Their finite-fault slip distributions exhibited uniform and circular shaped down-dip rupture propagations close to earthquake foci at depths from 10 to 15 km. The most recent (prior to 2017) activity in the study area involved a series of moderate earthquakes in 2004-2011, some of which occurred within just a few kilometers from the epicenter of the 2017 main shock (Table 1).

Table 1. Information on the source parameters of moderate earthquakes (4.7<M<5.5) that occurred near the 2017 main shock since 2004. The last column gives the reference of the determined fault plane solution, as 1: Pondrelli et al., 2007, 2: Pondrelli et al., 2011, 3: GCMT solution

Date DD/MM/YYYY	Time hh:mm:ss	Lat (◦)	Lon (◦)	Depth (km)	Mw	Length (km)	Width (km)	Slip (m)	Focal mechanism (◦) (strike/dip/rake)	ref
03/08/2004	05:33:38	36.830	27.847	15.0	4.7	2.95	3.20	0.03	266/56/-74	1
03/08/2004	13:11:34	37.020	27.720	15.0	5.2	5.25	4.79	0.07	264/49/-73	1
04/08/2004	03:01:09	36.902	27.772	15.0	5.5	7.41	6.09	0.13	271/65/-77	1
04/08/2004	04:19:50	36.850	27.776	15.0	5.2	5.25	4.79	0.07	255/67/-93	1
04/08/2004	14:18:51	36.861	27.715	15.0	5.3	5.89	5.19	0.09	259/55/-83	1
10/01/2005	23:48:53	36.810	27.660	12.0	5.5	7.41	6.09	0.10	273/53/-97	2

11/01/2005	04:35:58	37.180	27.788	12.0	5.1	4.68	4.42	0.06	271/59/-84	2
08/05/2011	06:50:24	36.696	27.237	12.9	5.2	5.25	4.79	0.09	248/51/-86	3

In an attempt to investigate the role of the recent moderate magnitude seismicity in the 2017 main shock occurrence, we calculated the static Coulomb stress changes caused by the coseismic slip of the eight earthquakes with 4.7<M<5.5 listed in Table 1. Five out of these eight earthquakes occurred in August 2004 at a distance of 15-25 km from the 2017 main shock. We used their fault plane solutions (strike/dip/rake) and moment magnitudes (M_w) for calculating the source parameters. For calculating the coseismic slip (u) we applied the scaling laws (Wells & Coppersmith, 1994) for the fault length, and the relation $u=Mo/\mu A$, where A is the rupture area and μ is the shear modulus for crustal faults (3×10^{11} dyn/cm2, Hanks & Kanamori, 1979), while the M_0 is the seismic moment provided by GCMT.

The static Coulomb stress change, ΔCFF, in a simplified form to account for pore pressure effects, is given by (King et al., 1994):

$$\boldsymbol{\Delta CFF = \Delta\tau + \mu'\Delta\sigma_n} \quad (1)$$

where $\Delta\tau$ is the change in shear stress onto the fault plane, considered positive in the slip direction, $\Delta\sigma_n$ is the normal stress changes, considered positive in unclamping, and μ' is the effective coefficient of friction, taken equal to 0.4 as it has been widely accepted (Papadimitriou, 2002; among others). Figure 4 shows the cumulative stress transferred by these earthquakes for a receiver fault of the main shock, calculated at a depth of 10 km, which is considered as the nucleation depth of the local seismogenic layer. We found that the main shock epicenter is located inside a stress-enhanced area, where the positive stress changes

have taken values >0.01 bar. Although tiny, we consider this prior activity as encouraging the 2017 seismic excitation.

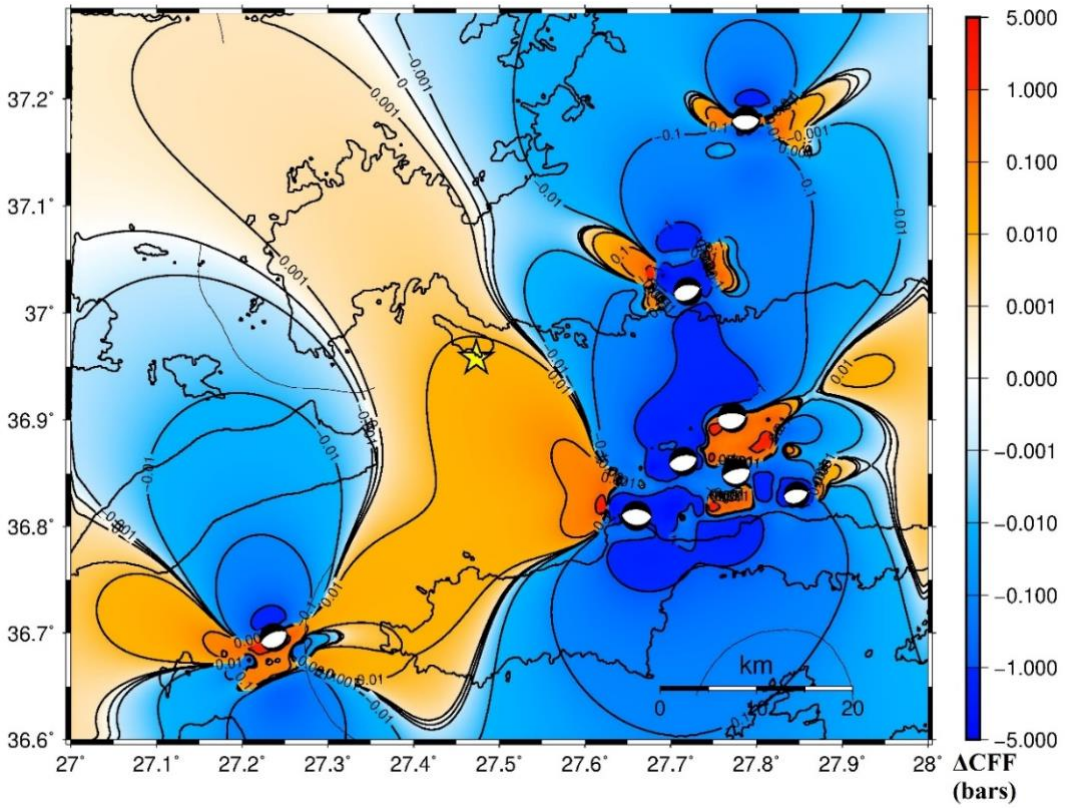

Figure 4. Stresses imparted by the eight moderate earthquakes that occurred at a distance of ~20 km from the 2017 main shock epicenter, resolved according to the GCMT fault plane solution of the 2017 main shock (strike/dip/rake= 278°/36°/-82°) at a depth of 10 km. The focal mechanisms are plotted as equal area lower hemisphere projections at the epicenter of each shock. The values of the static Coulomb stress change (ΔCFF) are given in bars according to the color scale in the right hand side of the figure. The main shock epicenter from 2017 is denoted by yellow star.

3 Seismicity relocation, fault plane solutions and spatiotemporal evolution

3.1 Relocation of the aftershock seismicity

The data recorded by the regional seismological networks often contain drawbacks related to the fact that the routine analysis offers fast and large number of locations and magnitudes

in almost real time, traditionally used for civil protection purposes (information and rapid response). The location procedure for a seismic sequence in the routine analysis is based on the manually picked and automatically revised marked P- and S-phase arrivals. Particularly the first hours and days, a number of lower magnitude earthquakes is missing as their body wave arrivals are obscured due to the high occurrence rate of the bigger events.

For the fault geometry constraint and associated tectonics, we relocated the aftershocks that occurred between July 20 and October 31, 2017. The rate of aftershock occurrence became very low in the following period. We used the arrival-time picks of the waveform data recorded by the Hellenic Unified Seismological Network (HUSN, doi:10.7914/SN/HL), the Kandilli Observatory and Earthquake Research Institute (KOERI, doi:10.7914/SN/KO), as well as arrival-time picks from the Disaster and Emergency Management Authority (AFAD, doi:10.7914/SN/TU) seismological networks. Aftershocks phase picks and waveforms from the three mentioned networks were gathered by the Geophysics Department of the Aristotle University of Thessaloniki (AUTH, doi:10.7914/SN/HT) to constitute our data source. We used the recordings of 17 seismological stations being at distances up to 160 km (Fig. 5) for the aftershock relocation. The closest station (BDRM) to the earthquake sequence is located in a mean distance of 14 km from the aftershock area. The recordings of the regional stations at larger distances were not considered for the aftershock relocation, aiming to avoid interference of large lateral heterogeneities in the crustal model. During the study period

more than 1450 events with magnitudes M>1.4 were recorded by the three above mentioned seismological networks.

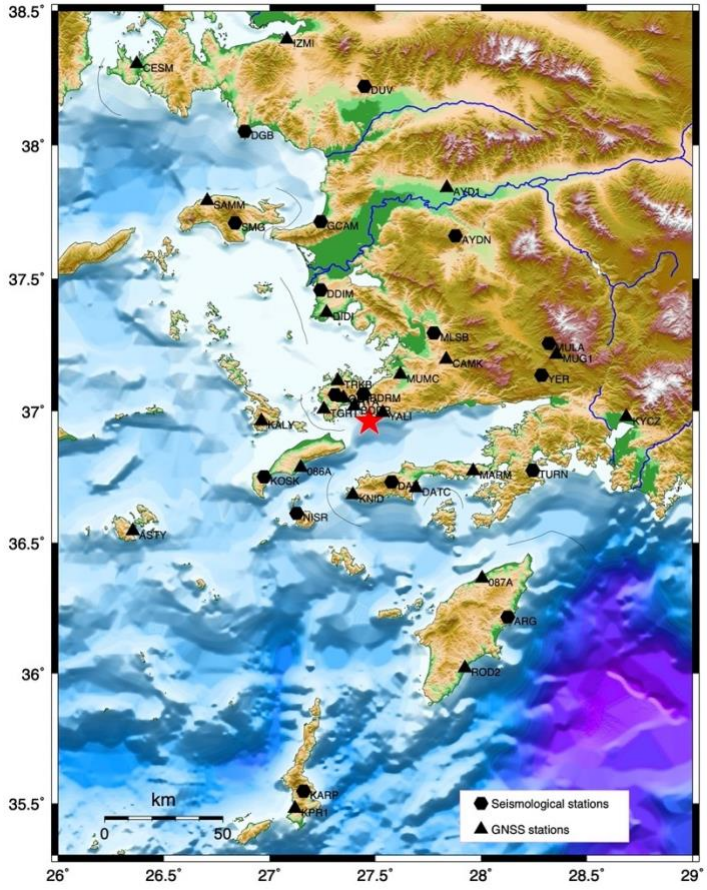

Figure 5. Black hexagons and triangles depict the geographical distribution of the 17 seismological and the 24 GNSS stations, the recordings of which were used for the seismic sequence location and the calculation of the surface deformation, respectively. The red star shows the main shock epicenter.

For our study purposes, to obtain a highly precise relocated catalog, we manually checked and repicked the P- and S-phase arrivals, when it was considered necessary. For the early aftershocks, we exerted an extra effort to add more data in the initial catalog, since the spatiotemporal behavior of the early aftershocks provide crucial information for the main rupture geometry and properties. There were 13312 P and 8260 S arrivals picked for 1298 events, from the stations illustrated in Figure 5. We used these picks to locate the earthquakes along with a proper software and a velocity model, an appropriate velocity ratio

and stations corrections, which adjust the lateral homogeneities in the path of wave propagation (e.g. Papadimitriou et al., 2017). The velocity model including 6 layers over a half space is given in Table 2 (Akyol et al., 2006) and was used along with a recalculated v_p/v_s ratio, which was found equal to 1.737 after applying the Wadati method (Wadati & Oki, 1933) to a data set of earthquakes with at least 10 S phases. The origin times of all earthquakes reduced to zero and the velocity ratio was calculated using a common plot of t_s-t_p versus t_p (Fig. 6), where t_s and t_p are the arrival times for the S and P wave, respectively. Given that the 1D velocity model accounts only for velocity variability with depth, we calculated corrections for each one of the seismological stations aiming to consider lateral heterogeneities as well. Time corrections range between -0.27 and 0.22 sec, with 12 (71%) of them in the range -0.1 +0.1 sec, evidencing that the 1D velocity model represents adequately the real crust structure. Using the phases from these stations and the corresponding corrections, the velocity model and the HYPOINVERSE computer program (Klein, 2002), aftershock location was achieved, with spatial errors in these calculations of the order of a few kilometers.

Table 2. 1D velocity model for the seismicity relocation (after Akyol et al. 2006)

V_p (km/sec)	Depth (km)
4.70	0.0
5.10	1.5
5.80	3.0
6.00	5.0
6.30	15.0
6.40	21.0
7.80	29.0

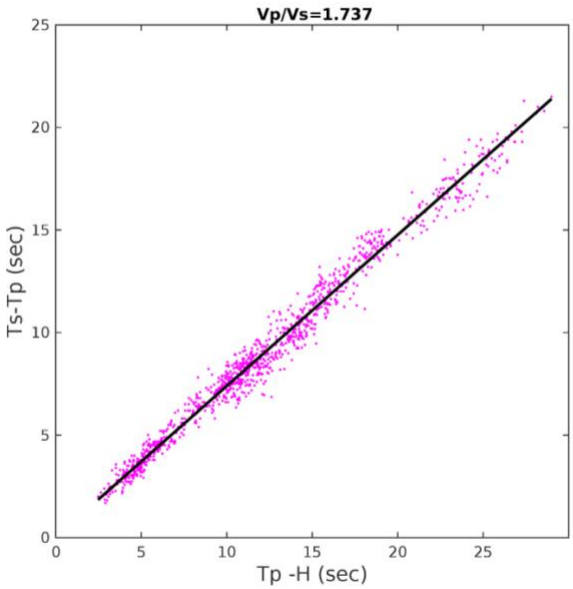

309

310 **Figure 6.** V_P/V_S ratio for the aftershock sequence resulted from the linear fit of t_P-t_S versus
311 t_p

312 After the initial location, a double difference algorithm was applied for the relocation
313 (Waldhauser & Ellsworth, 2000; Waldhauser, 2001), followed by cross correlation of the
314 waveforms in the time domain (Schaff & Beroza, 2004; Schaff & Waldhauser, 2005). The
315 final catalog comprises 1134 events recorded at five or more stations. The lower

magnitude is 1.4 and by applying the goodness of fit method (Wiemer & Wyss, 2000) at the 95% confidence interval the completeness threshold was found equal to 3.1 (Fig. 7).

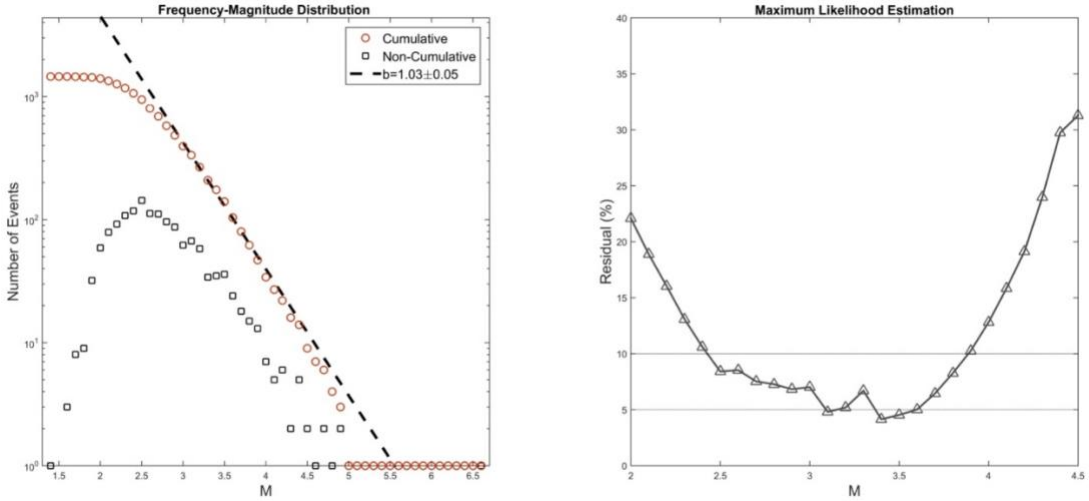

Figure 7. Identification of the completeness magnitude of the aftershock sequence: **(a)** cumulative and incremental frequency as a function of the magnitude. **(b)** Goodness of fit approximation. The M3.1 is adopted as the magnitude threshold given that at this point the residual drops below 5%.

Location errors derived by the hypoDD software using the LSQR approximation are of the order of a few meters, these values, however, have no physical meaning (Waldhauser, 2001). In order to estimate the achieved accuracy, an error analysis was performed in X, Y and Z directions, by applying a bootstrap resampling method (Efron, 1982). Figure 8 shows the histograms of the errors in each direction. The data are divided in those relocated using both cross correlation and phase picking (red color), and those relocated using only phase picking (blue color). One can clearly observe that cross correlation results significantly improve the relocation accuracy. The mean values of the errors in the X, Y and Z directions are 575 m, 373 m, and 452 m, respectively. There is a considerable difference between the two horizontal errors, which is probably due to the spatial distribution of the stations in the N-S

direction. The data accuracy as assessed by the aforementioned calculated errors is sufficient to adequately describe the aftershock distribution.

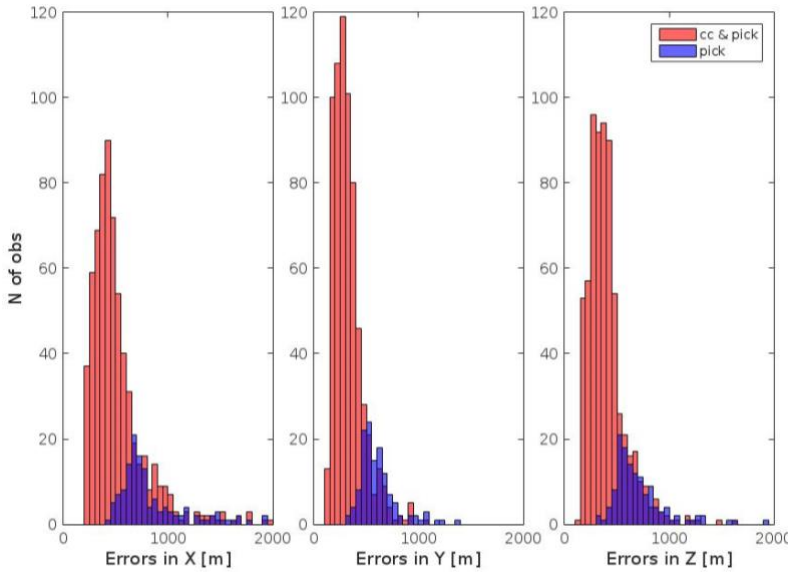

Figure 8. Histograms of the errors calculated by a resampling bootstrap method in the three directions X, Y, and Z., for data relocated by both, cross correlation (cc) and phase picking (red color) and data relocated using only phase picking (blue color).

3.2 Moment tensor solutions

We computed moment tensors for earthquakes with ML≥3.5 using waveform inversion implemented in the ISOLA package (Sokos & Zahradnik, 2008, 2013), and adopted solutions provided by GCMT and GFZ (Table 3). They concern aftershocks (either on or off fault aftershocks) located close to the main shock epicenter (given in the first row of Table 3) as well as the adjacent seismicity clusters (Fig. 9). We calculated Green's functions for stations located within 150 km from the earthquake epicenter using a 1D velocity model (Akyol et al., 2006, Table 2). The inversion was performed for a deviatoric moment tensor and the waveforms are filtered to frequency range of 0.04-0.08 Hz. To assess the quality of the computed moment tensors, we consider a number of quality factors as described by Sokos & Zahradnik (2013). Briefly, we checked the spatio-temporal variability of the focal mechanism (FMVAR), and obtained a mean value of 14. Then, the surface of the area in the space-time plot occupied by the solutions within a given correlation threshold, normalized

by the total area of the investigated space-time region (STVAR), is calculated with a mean value of 0.2. Additionally, we considered on average eight stations for each inversion that resulted in solutions with a mean double couple (DC) of 81%, and mean condition number (CN) of 3. The finally selected fault plane solutions are shown as lower hemisphere equal area projections in Figure 9 and are plotted at the epicenter of each earthquake. The size of each beach ball is proportional to the earthquake magnitude.

Table 3. Information on the fault plane solutions determined by GCMT (noted by number 1 in the last column of the table), determined in this study (2), and by German Research Centre for Geoscience – GFZ (http://geofon.gfz-potsdam.de/eqinfo/list.php) (3)

S/N	Date YYYY/MM/DD	Or. Time hh:mm:ss	Lat. (°)	Lon. (°)	Depth (km)	M_w	Strike (°)	Dip (°)	Rake (°)	source
1	2017/07/20	22:31:10.76	36.9580	27.4730	13.53	6.6	278	36	-82	1
2	2017/07/21	01:25:34.74	36.9813	27.4191	12.67	4.1	258	81	-65	2
3	2017/07/21	01:35:44.39	36.9269	27.5850	11.55	4.5	214	59	-171	2
4	2017/07/21	01:38:49.53	36.9272	27.5039	8.40	4.7	237	28	-148	2
5	2017/07/21	02:12:35.12	36.8641	27.3559	11.71	4.7	253	46	-112	3
6	2017/07/21	03:59:02.31	36.9220	27.6224	11.58	4.4	256	46	-85	2
7	2017/07/21	05:04:00.52	36.9238	27.6435	10.87	5.0	267	55	-73	1
8	2017/07/21	05:13:59.30	36.9060	27.6140	2.67	4.3	259	51	-97	3
9	2017/07/21	05:52:13.96	36.9818	27.3443	14.65	4.1	240	53	-93	3
10	2017/07/21	09:55:53.94	36.9206	27.6921	13.32	4.4	269	49	-89	2
11	2017/07/21	17:09:50.86	36.9350	27.3267	10.65	5.0	267	55	-73	1
12	2017/07/22	17:09:21.90	36.9530	27.3520	4.40	4.4	255	56	-97	2
13	2017/07/30	07:02:13.80	37.0140	27.5970	8.40	4.2	243	59	-99	2
14	2017/07/30	17:51:18.76	36.9679	27.6597	11.08	4.8	278	62	-91	2
15	2017/08/07	05:18:48.23	37.0004	27.6253	14.04	4.9	261	51	-107	2
16	2017/08/07	05:44:25.62	37.0044	27.6490	9.43	4.2	267	50	-99	3
17	2017/08/07	18:25:57.98	36.9865	27.6448	12.30	4.0	283	62	-109	2
18	2017/08/08	01:46:20.04	36.9900	27.6409	13.53	4.1	276	64	-82	2
19	2017/08/08	07:42:20.83	37.0067	27.6505	13.84	5.3	270	48	-81	1
20	2017/08/13	11:16:52.28	37.1204	27.7227	10.84	5.0	271	55	-98	2
21	2017/08/13	12:28:15.04	37.1394	27.7147	15.19	4.5	263	34	-105	2
22	2017/08/13	16:31:21.82	37.1394	27.7071	8.16	4.0	272	61	-94	2
23	2017/08/13	16:35:22.59	37.1380	27.7355	14.75	4.4	278	42	-93	3
24	2017/08/13	17:09:06.56	37.1340	27.7156	12.39	4.0	271	20	-119	2
25	2017/08/14	02:43:48.86	37.1401	27.7251	14.78	4.6	279	32	-88	3
26	2017/08/18	12:47:32.61	36.9223	27.6482	12.33	4.2	283	58	-86	2
27	2017/08/18	14:10:48.27	36.9328	27.6490	7.15	4.4	278	65	-88	2
28	2017/09/16	08:33:56.02	37.1435	27.7294	10.58	4.4	196	68	-166	2
29	2017/09/24	16:57:16.93	36.9499	27.3374	9.77	4.2	251	33	-99	2
30	2017/10/24	09:36:24.58	36.9753	27.4261	11.02	4.8	270	38	-109	1
31	2018/09/10	15:07:10.00	36.9830	27.7680	2.80	4.6	262	51	-95	3
32	2019/05/28	05:27:47.23	36.9591	27.6802	7.64	4.7	270	47	-110	1

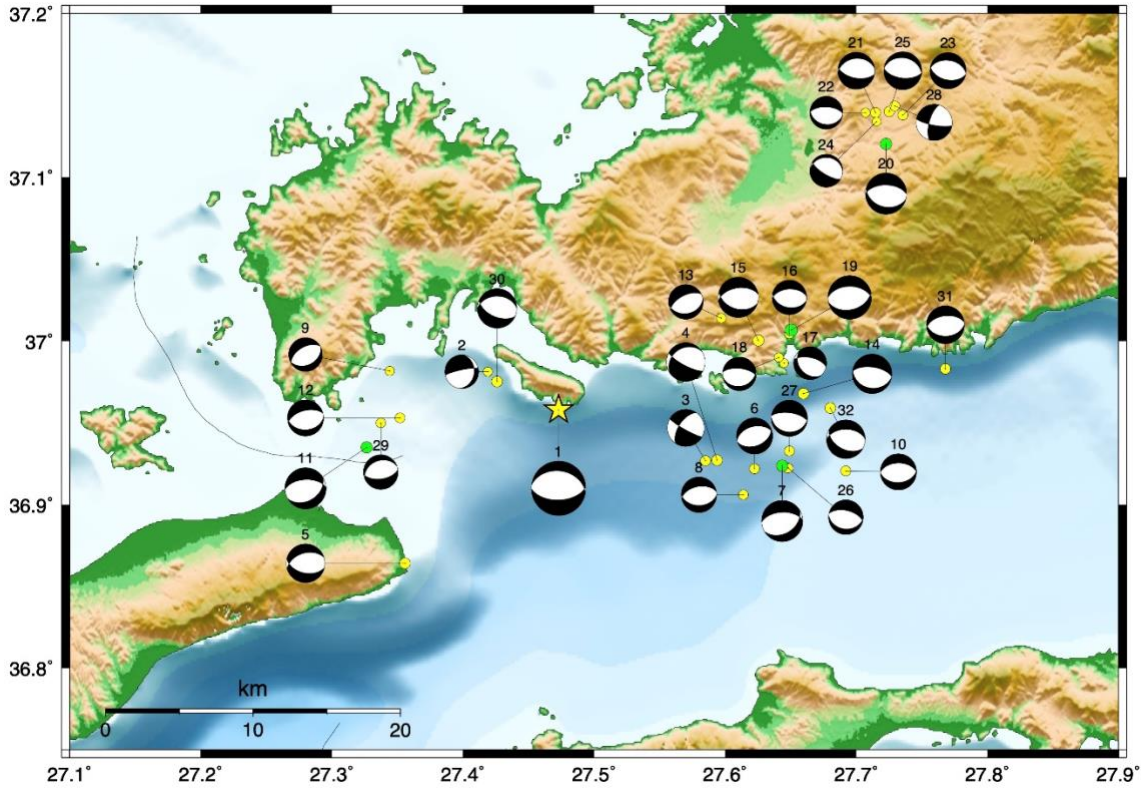

Figure 9. Fault plane solutions of the main shock (the epicenter of which is denoted by the yellow star) and the aftershocks listed in Table 3, shown as equal area lower hemisphere projections. The number on the top of each beach ball corresponds to the number given in the first column of Table 3.

Both Table 3 and Figure 9 evidence the prevalence of the normal faulting, with E-W striking nodal planes in full agreement with the N-S regional extensional stress field. This faulting type characterizes foreshocks onto or very near the main rupture, as well as the off fault aftershocks forming two clusters, to the east and northeast of the main shock. The appearance of a slight strike slip component in some aftershocks of lower magnitude cannot be ruled out and provides the basis for considering complexity of the faulting mechanics, but

there is not adequate information (small number of solutions) on which a robust discussion can be built.

3.3 Spatiotemporal evolution of the aftershock seismicity

The epicenters of the 1134 relocated earthquakes are plotted on the map of Figure 10a. They are distributed in an almost east-west oriented seismic zone with over ~40 km length, which is larger than the expected fault length for an M6.6 main shock, as it is given from well-known scaling laws connecting main shock magnitude and rupture length (Wells & Coppersmith, 1994; Papazachos et al., 2004; among others). The almost E-W alignment is generally consistent with the dominant N-S extension. The refined relocation of the aftershocks improves our knowledge on the geometry and kinematic details of the activated structures. The identification of as much as possible smaller magnitude aftershocks enhance the detailed analysis of the spatiotemporal evolution of the sequence. In the strike parallel cross section (Fig. 10b) along the line PP', an area of more than 10 km in length around the main shock epicenter is devoid of aftershocks, implying an asperity, at the edges of which the aftershocks are densely concentrated. In the strike normal vertical cross section along the line NN' (Fig. 10c) a north dipping trend is observed, coherent with the one nodal plane of the GCMT solution. The main shock is located in the deeper part of the north dipping aftershock zone. The histogram, of the aftershocks focal depths (Fig. 10d) shows that the vast

majority of the aftershocks are distributed at depths between 7 and 15 km, consistent with the brittle crust thickness of the back arc Aegean area.

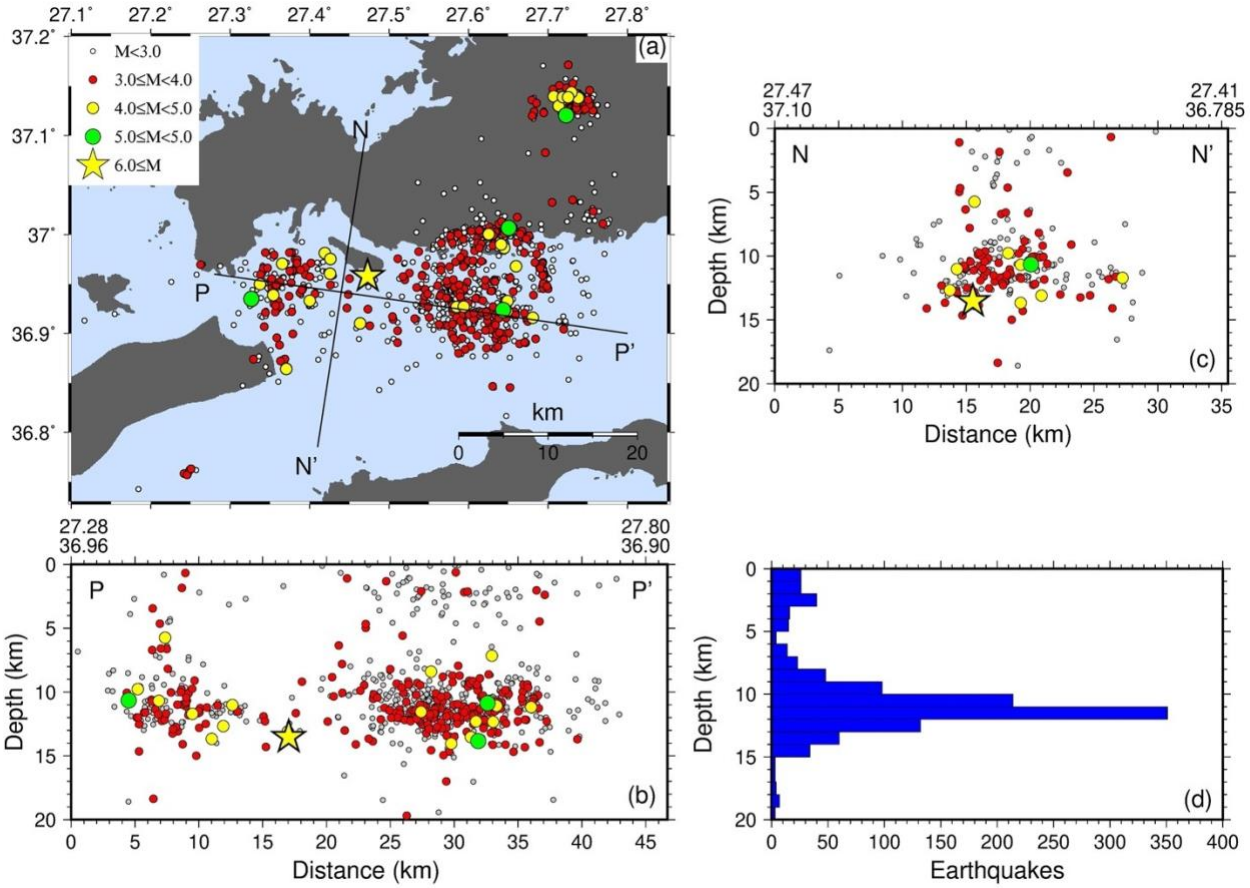

Figure 10. (a) Map showing the epicentral distribution of the relocated aftershocks. The yellow star depicts the main shock epicenter. Earthquake epicenters are colored as a function of magnitude according to the scale. **(b)** Strike parallel cross section of the relocated aftershocks along the line PP'. **(c)** Strike normal cross section of the relocated aftershocks along the line NN'. **(d)** Histogram of the focal depths of the relocated aftershocks.

A spatiotemporal distribution (Fig. 11) in an almost W-E direction (along the line PP' of Fig. 10a), shows that the seismic activity expanded almost immediately in the entire aftershock zone. From this distribution we may observe distinct characteristics, as that in the first day of the sequence seven earthquakes of M>4.0 (the main shock including) occurred in the western part and only four in the eastern part. Instead, the number of the lower magnitude earthquakes is significantly higher in the eastern part. This might be rather attributed to the

fact that large fault patches were failed in the larger magnitude aftershocks in the western part than to the obscurement of the waveforms of smaller aftershocks by the larger aftershocks' waveforms. After the first two days, the seismic activity in the western part considerably diminished. Around the main shock epicenter, the aftershock density is clearly less dense, implying stress free area in a fault patch where the maximum coseismic slip took place. This steadily remained free of aftershock epicenters in the entire 100-day span of our data set. It is worth to note that two M>5.0 aftershocks (green circles) that occurred on the same day with the main shock, are located at the two opposite edges of the activated area, implying triggering effects at the fault tips, where the stress concentrations receive the highest positive values.

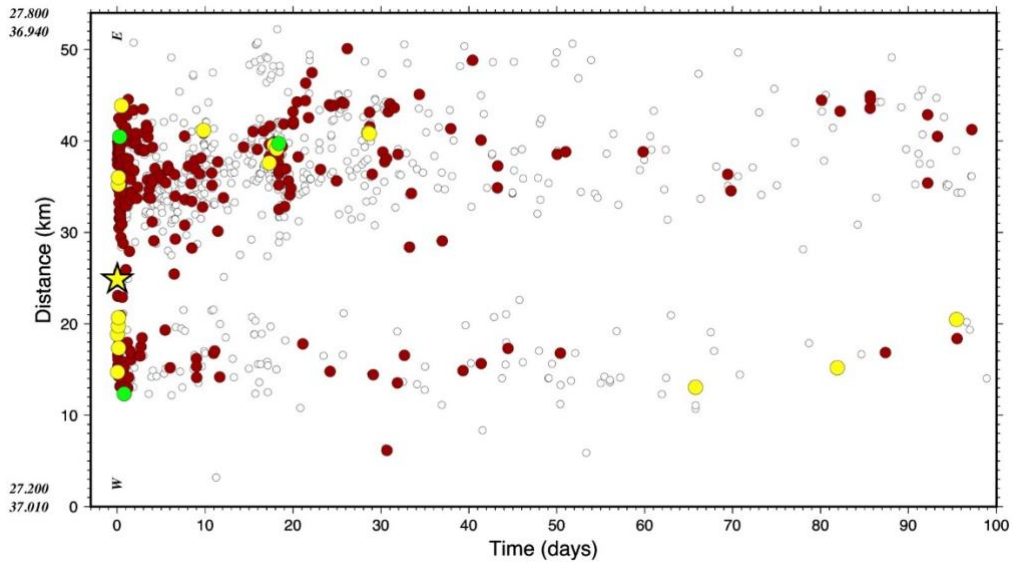

Figure 11. Spatiotemporal aftershock distribution along an almost west-east direction (along the line PP' shown in the map of Fig. 10a). Symbols are as in Figure 10.

In the eastern part of the aftershock zone (Fig. 11) the seismic activity was higher, hosting the largest aftershock (M5.3) of the sequence, that was triggered eighteen days later and was accompanied by its own aftershocks (increased rate of the M>3.0 aftershocks, red circles). The intense activity on the eastern cluster is attributed, as will be shown below, to the positive Coulomb stress changes at this location, due to the main shock slip. To the N-NE of the main activity (Fig. 10a), a second distinctive cluster originated four days after the main

shock occurrence with the activity peaked twenty days afterwards. It exhibits a high spatial concentration, with the maximum magnitude earthquake of M=5.0, and several M>4.0 events.

Figure 11 shows that during the days 17-21 after the main shock occurrence (06-10 August 2017) a cluster of earthquakes in the easternmost part of the aftershock zone was formed. The stronger earthquake (M5.3) of this cluster occurred on 8 August 2017. A second distinctive cluster, which was not included in the space time plot because it is out of the main aftershock zone, took place in the period 12-17 August 2017. Aiming to examine the spatial features of these two clusters, all the aftershock epicenters of the period 06-16 August were plotted on the map of Figure 12a. The first cluster is developed along the coasts of Bodrum peninsula, elongated in an almost E-W direction, with a total length equal to 11 km. In addition to the M5.3 earthquake, three more earthquakes with M>4.0 are included in this cluster and several with M>3.0. A cross section normal to the cluster's orientation (Fig. 12b) along the line N1N2 shown on the map of Figure 12a, striking at N170°, shows that the focal depths are distributed in the range of 8-14 km. The earthquakes of this cluster occupy the left part of Figure 12b and show a clear dip to the north in agreement with the one nodal plane of the fault plane solutions (Table 3). A few days later, the second cluster formed at a distance of about 15 km NNE of the main rupture zone (Fig. 12a), with the stronger earthquake in this cluster having a magnitude of M5.0, and six more earthquakes of M>4.0. The epicenters are all tightly concentrated in space, aligned along an east-west orientation, forming a zone with length of about 6 km. A cross section along the line N3N4 in the direction N185° shows a depth distribution (9-13 km) similar with the previous cluster, one convincing indication for the thickness of the brittle layer and the depth of seismicity pick. The hypocenters indicate an activated fault dipping to the north, in agreement with the one

of the nodal planes of the three available focal mechanisms of this cluster (Table 3 and Fig. 9).

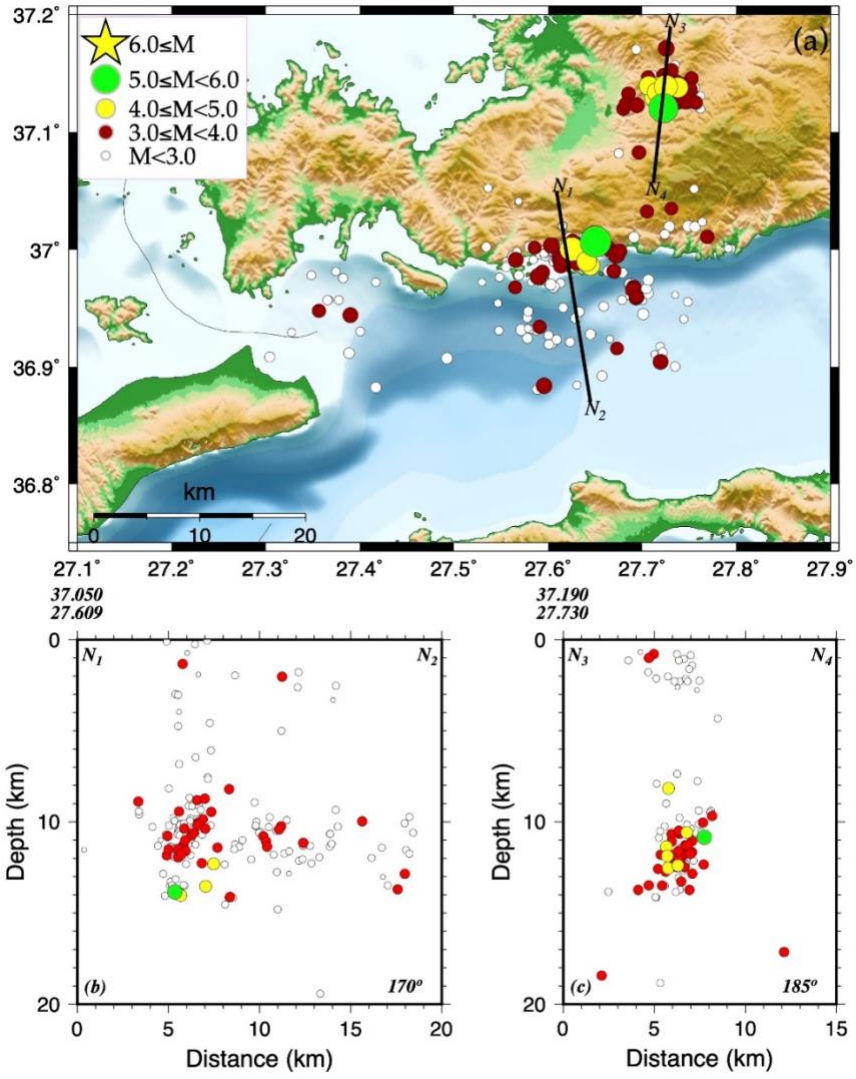

Figure 12. (a) Spatial distribution of the seismicity forming two distinct clusters, namely the eastern and northeastern ones. **(b)** Vertical cross section of the seismicity encompassed in the eastern cluster along the line N_1N_2 shown in the map of Fig. 12a. **(c)** Vertical cross section

of the seismicity encompassed in the northeastern cluster along the line N_3N_4 shown in the map of Fig. 12a.

4 Geodetic observations of the coseismic surface

The geodetic data used in the current study consist of two types of coseismic observations – deformation maps with areal coverage derived by applying the Differential Interferometry Synthetic Aperture Radar (DInSAR) technique, and pointwise displacements measured by Global Navigation Satellite System (GNSS) and available in the literature.

4.1 Surface displacement obtained with Differential Satellite Interferometry (DInSAR)

Proven by numerous examples from the last several decades (Massonnet et al, 1993, among others), the application of the technique of satellite interferometry with synthetic aperture radar (InSAR) plays a notable role in defining the field of surface deformations caused by moderate to strong earthquakes. The special range of deformations is also used alone or in a join inversion for modelling of the causative fault. To estimate the surface displacement by Differential InSAR (DInSAR), C-band satellite radar images with wavelength of ~5.55 cm, acquired by the Sentinel-1 mission of the European Space Agency (ESA) have been used. The data are available on the ESA's data hub (Copernicus Sentinel Data, 2021). The used in the current study images are in Interferometric Wide (IW) swath mode, in Single Look Complex (SLC) format with average special resolution of 3x22 m (range x azimuth). We combined two coseismic pairs of images with VV polarization, namely one pair from the ascending track 131 from the dates 18/7/2017-24/7/2017, and a second pair of the image from the descending track 36 from dates 18/7/2017-30/7/2017. The ESA's Sentinel Application Platform (SNAP) was used to process the radar interferogram couples. The Shuttle Radar Topography Mission (SRTM; EROS, doi:/10.5066/F7PR7TFT) 1 arc-second (30-m resolution) Digital Elevation Model (DEM) was applied for the topographic phase removal. Multilooking (6 range x 2 Azimuth looks) and a Goldstein filter (Goldstein & Werner, 1998)

are applied to the received wrapped interferograms (Fig. 13) aiming to reduce the noise and to support the unwrapping of the radar phases.

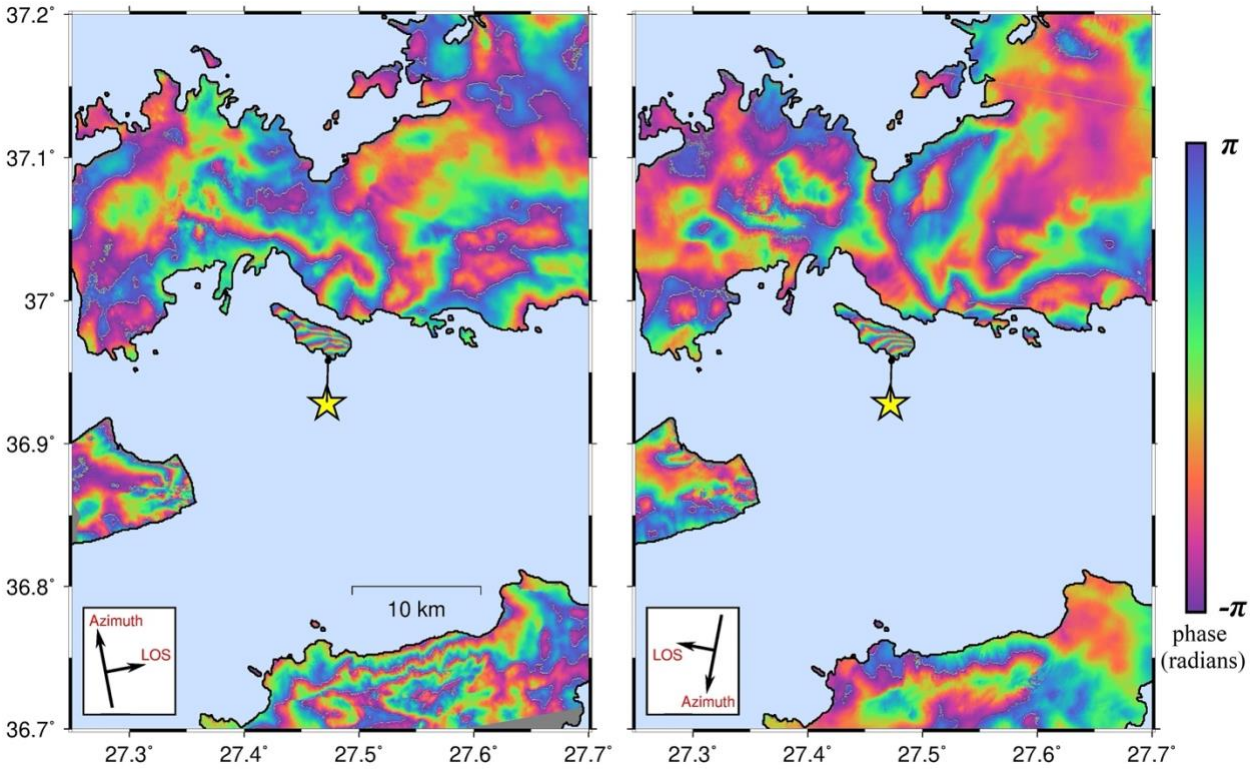

Figure 13. Wrapped coseismic Interferograms: (left) between 18 and 24 July 2017 calculated from images acquired in Sentinel-1 ascending track № 131, and (right) between 18 and 30 July 2017 calculated from images acquired in descending track № 36.

Both resulted wrapped interferograms, ascending and descending, show six-seven fringes over the area of the Kos Island associated with the coseismic surface displacement caused by the main rupture, postseismic motions and the stronger aftershocks within the timespan of the interferograms. The usage of C-band Sentinel-1 radar images reveals a corresponding approximate displacement in the line-of-sight (LOS) direction to the slant-range looking satellite at the level of more than 16-19 cm (six-seven times the half wavelength). Strong additional influence on the patterns in Figure 13, most probably due to atmospheric effects (Dogru, 2020), is also clearly visible and must be considered as an additional distortion on the deformation values over the area of interest. The correction for atmospheric delays provided by the Generic Atmospheric Correction Online Service (GACOS, Yu et al., 2017) was

implemented by the KITE module of Pyrocko package on a later step. The Minimum Cost Flow (MCF) method (Chen & Zebker, 2000) was applied with the SNAPHU algorithm for phase unwrapping and receiving the total amount of displacements in LOS directions.

The unwrapped interferograms were further processed with the KITE software (Isken et al., 2017), so that the unwrapped phase is transformed into surface displacement and subsequently subsampled (Fig. 14). The quadtree subsampling algorithm (Jónsson et al., 2002) is applied with a root mean square (RMS) threshold of 0.1 and a minimum tile size of 0.01o. The approach is used in order to obtain a computationally efficient displacement scene where areas with high displacement gradients are sampled with a higher resolution, whereas sample density is lower in areas with low displacement gradient. The variance-covariance matrix of the subsampled data was estimated after selecting a noise window to quantify the noise contribution to the data. Finally, the crustal model of Akyol et al. (2006)

(Table 2) was used to estimate static displacements using the PSGRN/PSCMP backend (Wang et al., 2006).

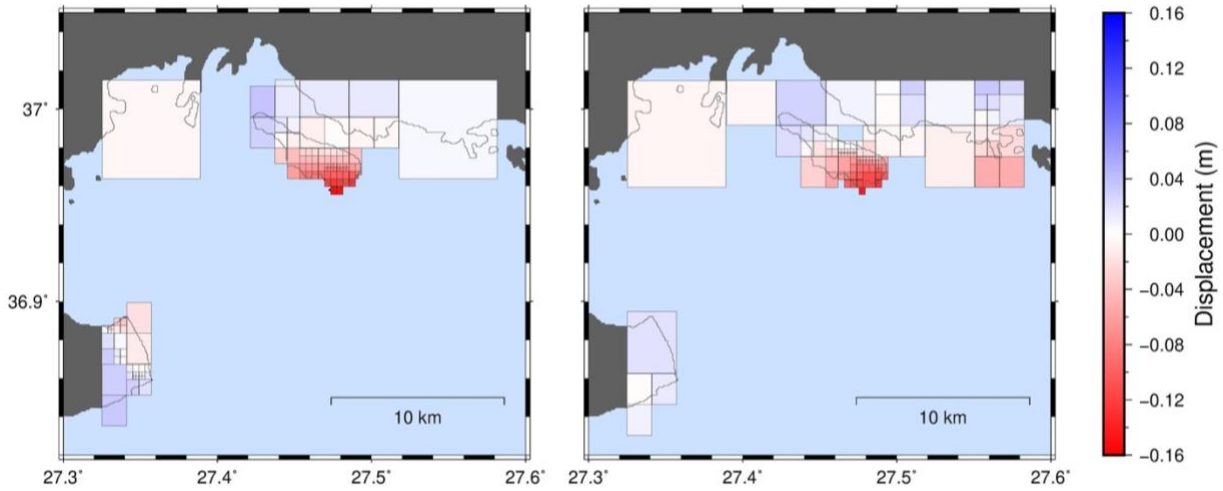

Figure 14. Unwrapped ascending and descending coseismic displacement maps showing the sampling used in the first stage of fault geometry modelling

4.2 GNSS data used in the fault modelling procedure

The displacement GNSS vectors from all available permanent GNSS network in the area used here are those estimated by Tiryakioglu et al. (2018) and Ganas et al. (2019) (Table 4, Fig. 5).

Table 4. Components of coseimic displacement at GNSS stations (sources are denoted as 1: Ganas et al. (2019) or 2: Tiryakioglu et al. (2018) and modelled displacements (see Section 6)

station	Measured displacements			source	Modelled displacements		
	dE(mm)	dN(mm)	dU(mm)		dE(mm)	dN(mm)	dU(mm)
086A	-9±3	-10±3	16±9	1	-10	-10	6
087A	-3±3	-5±3	-8±9	1	1	-6	0
ASTY	-2±4	-1±4	2±12	1	-1	-1	1
AYD1	2±4	4±4	-7±15	2	1	6	-1
BODR	-38±9	160±9	119±22	2	-20	126	36
CAMK	2±5	28±6	28±21	2	12	24	1
CESM	0±3	1±3	-6±11	2	0	1	0
DATC	10±5	-32±5	8±15	1	8	-49	6
DIDI	-5±5	19±5	2±15	1	-4	19	0

FETH	-1±3	2±3	-5±13	2	0	0	1
IZMI	1±3	1±3	-2±10	2	0	2	0
KALM	-3±4	0±4	11±12	1	1	0	5
KNID	-20±4	-50±4	-2±16	2	-18	-67	-3
KPR1	0±4	-4±4	5±12	1	0	-2	0
KYZC	12±9	6±9	10±30	2	0	0	1
MARM	6±3	-2±3	6±10	2	-4	-2	5
MUG1	0±5	-4±5	6±15	1	1	2	1
MUMC	23±2	69±3	4±10	2	21	79	8
ORTA	-39±2	100±3	15±9	2	-21	84	18
ROD2	2±2	-6±2	6±10	2	1	-5	0
SAMM	-4±4	1±4	6±12	1	-1	2	0
TGRT	-9±3	25±3	1±11	2	-2	24	9
TRKB	-25±2	65±2	3±9	2	-17	60	10
YALI	7±3	153±3	7±11	2	10	154	15

Tiryakioglu et al. (2018) used data from 20 GNSS stations (15 continuous stations and 5 campaign-surveyed stations). The permanent stations were distributed in the borderlands of Greece and Turkey. The GNSS campaign data were acquired during five measurement sessions between 2002 and 2013. To obtain the displacement values, the campaign stations were re-measured three days after the main shock (on 24 July 2017). The coordinates of all GNSS stations were estimated using GAMIT/GLOBK software, based on the rapid GNSS products. Ganas et al. (2019) used the data from the Tiryakioglu et al. (2018) paper, however they additionally determined displacements from other GNSS stations. They determined the GNSS displacement vectors using the Precise Point Positioning (PPP) technique in the GIPSY/OASIS II software (ver. 6.4). To obtain the highest precision of estimation, the authors used final GNSS orbital and clock products.

Based on the data from the aforementioned articles, it can be noted that the closest GNSS station (YALI) was located about 7 km from the main shock epicenter, and the farthest station (CESM) was about 178 km away. Considering the measured GNSS displacements, the

largest horizontal and vertical deformations occurred for the BODR station (about 10 km far from the main shock epicenter).

5 Joint inversion for fault geometry modelling

One pivotal aspect in examining aftershock activity, surface displacements, and coseismic stress changes is the calculation of a fault model geometry and estimation of the coseismic slip distribution of the main rupture, either uniform or variable. In the current study, the fault modelling was performed in two stages (Fig. 15). Firstly, using regional waveforms, GNSS displacement vectors, and DInSAR surface deformations, a rectangular fault with uniform slip respecting the Okada (1992) definition was proposed. Then, the second step aimed to define the fault geometry with a variable slip distribution using finite join inversion based on the chosen geodetic data and the aftershock distribution. The modelled fault was used to calculate the coseismic stress changes and the surface displacements. All the data preparation and the modelling were handled with the various software tools under the Pyrocko toolbox (Heimann et al., 2017).

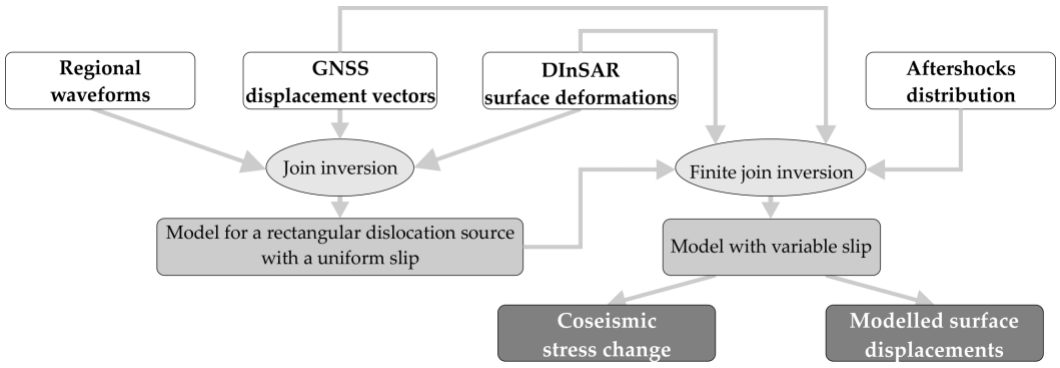

Figure 15. Modelling strategy – input data, phases of processing and output products

The waveforms recorded by eleven broadband regional stations belonging to the Greek seismographic network (HUSN) and Turkish networks (AFAD and KOERI, see Section 3) in distances ranging between 155 and 465 km have been used in this study (Fig. 16). The stations were chosen aiming to achieve a satisfactory azimuthal coverage. The inversion was performed in the time domain, using the complete waveform, and tapered with a flat frequency response of 0.005-0.02 Hz, falling to zero at 0.003Hz and 0.03Hz, defined as $f_{min}/1.5$ and $fm_{ax}*1.5$. The crustal model of Akyol et al. (2006) (Table 2) was assumed for the

calculation of the Green's functions using the QSEIS backend (Wang, 1999), through the Fomosto tool of the Pyrocko package.

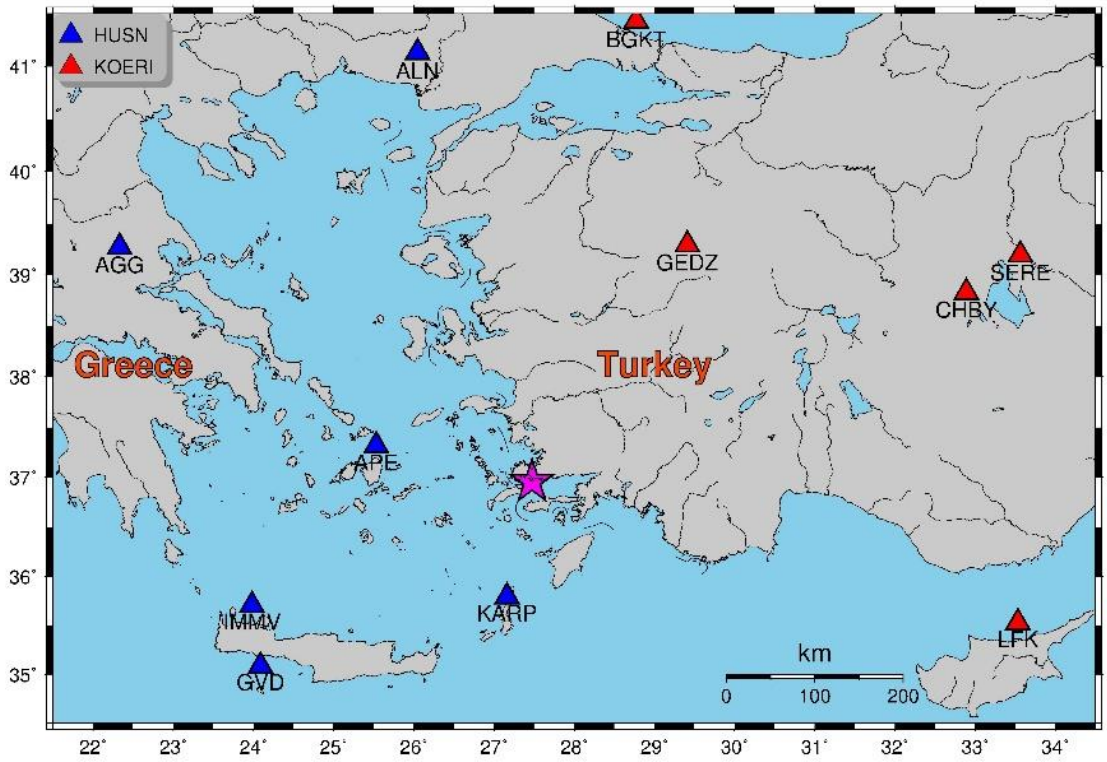

Figure 16. Seismological stations from the Greek (HUSN, blue triangles) and Turkish (KOERI, AFAD, red triangles) national networks, used in the joint inversion for the uniform slip model. The star denotes the main shock epicenter.

The optimization for the initial uniform slip source was performed using all available datasets (regional waveforms, displacement field from DInSAR and displacement vectors from GNSS) with the GROND software (Heimann et al. 2018), which performs a Bayesian bootstrap-based probabilistic joint optimization procedure. The models are evaluated based on the L2-norm misfit (e_{norm}) for each target *i* of a given target group (waveform, DInSAR or GNSS)

$$|e_{norm}| = \sqrt{\frac{\sum(w_i \cdot |d_{obs,i} - d_{synth,i}|)^2}{\sum(w_i \cdot |d_{obs,i}|)^2}}, \quad (2)$$

where d_{obs} and d_{synth} are the observed and synthetic data, respectively, and *w* is the target weight. The global misfit when combining multiple target groups is the RMS of the

normalized target group misfits. A number of parallel bootstrapping on model misfits is performed to ascertain model uncertainties.

Following the Okada (1992) definition of a simplified rectangular source by nine parameters, we assumed a rectangular uniform slip source and performed the optimization for the fault dimensions (length, width), position (depth of upper fault edge, shift in northern and eastern direction of the center of the upper edge from the relocated hypocenter), faulting characteristics (strike, dip, and rake angles) and a uniform slip value. The aftershock spatial distribution (Section 3) implies a north-dipping fault and the moment tensor of GCMT (and other institutions) points to an almost E-W strike. We thus constrained the parameters searching for a north dipping fault, striking at 270±30º.

For the first stage of the optimization, models were randomly selected from the possible model solutions for 5000 iterations, and they were evaluated and formed a high-score list. For the next 50000 iterations, a directed sampling of the high-score list was accomplished. This was based on a normal distribution that is determined from the standard deviations of high-score models multiplied by a logarithmically decreasing scaling factor, which in our case started from 1.5 and ended at 0.25. A set of 200 bootstrapping chains (Daout et al., 2020; Foumelis et al., 2021) were carried out for estimating the uncertainties of the parameters. The results and uncertainties for the uniform slip model are presented in Table 5 for the best fitting model (Fig. 17 – dashed green rectangle).

Table 5. Parameters estimated for the uniform slip model with their standard deviation (std) values. The north and east shift from the relocated epicenter (star in Fig. 17a) are denoted with (+) shift to the east and to the north.

Parameter (unit)	**Value ± std**
East Shift (km from epicenter)	0.9±1.3
North Shift (km from epicenter)	-8.4±1.0
Length (km)	15.4±2.7
Width (km)	9.3±1.7
Depth (km) (the upper middle point)	3.2±0.5
Strike (°)	286±8

Dip (°)	39±3
Rake (°)	-77±8
Slip (m)	2.1±0.4
M_0 (N·m)	9.92e+18
M_W	6.6

The optimization suggests a 15.4 km long slip patch of normal faulting, onto a plane striking WNW-ESE and dipping at 39°, with a slight left lateral component (rake=-77°). The faulting characteristics, position and dimensions, are in agreement to the aftershock distribution (Fig. 10a) as well as with several north-dipping proposed models (Karakostas et al., 2018; Karasözen et al., 2018 – uniform slip model; Ganas et al., 2019; Konca et al., 2019; Cordie et al., 2021, see Table S1). The same is also valid for the seismic moment, estimated as $M0=\mu \cdot A \cdot D$, μ being the shear modulus taken equal to 33GPa, A being the area of the fault, and D being the uniform slip, which corresponds to a moment magnitude of Mw6.6 ($Mw=2/3 \cdot log_{10} Mo-16.1$), (Hanks and Kanamori, 1979). The standard deviations (Table 5) as well as the model fits for waveform (Fig. S1) and static displacement (Table 4) targets indicate a good quality model to proceed to the variable slip inversion. The parameters correlation plot (Fig. S2) reveals that the position of the fault (east and north shift, depth) appears to be better constrained than the fault dimensions (length and width) which are more scattered. Since this is an intermediate step and the variable slip model was calculated for an extended version of this geometry, we deemed those results acceptable.

After defining the fault geometry and orientation, we used the geodetic data (DInSAR and GNSS) to infer the variable slip distribution using the BEAT software (Vasyura-Bathke et al., 2019; 2020). We extended the rectangular model by a factor of 0.8 along strike and 0.6 along dip (Fig. 17a – green rectangle) for including the entire area of aftershock activity. This resulted in 777 (37x21) rectangular patches with dimensions of 1x1 km^2. For each patch, two slip parameters were optimized, one in the strike parallel and one in the strike normal direction. A smoothing constraint was applied via a Laplacian regularization factor to weight down large differences in slip between bordering patches. The variable slip optimization on the extended area (Fig. 17a – dashed blue rectangle) reveals one main asperity where high slip values are concentrated with a maximum slip value equal to 2.3 m. The slip distribution

618 diminishes faster in the west part of the main asperity, whereas in the eastern part of the
619 main asperity values of 0.5 m can be observed up to the eastern limit of the extended fault
620 area (Fig. 17a, b). The contour of 0.5 m slip (Fig. 17a) forms a rather elliptical shape with the
621 lengths of major and minor axis equal to 32 km and 13 km, respectively. It encompasses a
622 total area of 306 km^2, which is capable to produce an earthquake of M6.6 according to the
623 known empirical relations (Wells and Copersmith, 1994; Papazachos et al., 2004).
624 Considering that this area represents the dislocation plane from where the accumulated
625 elastic strain was released during the main shock, the estimated seismic moment, which
626 results in $Mo=1.046 \cdot 10^{19}Nm$ and consequently to a moment magnitude M6.6, is in good
627 agreement with that estimated by moment tensors solutions of several institutions. The slip
628 distribution is comparable to that estimated by previous studies (Karasözen et al., 2018;
629 Konca et al., 2019 – north-dipping distribution, Table S1) and is rather different from the slip

distribution defined by Tiryakioglou et al. (2018), where multiple slip patches are evident and maximum co-seismic slip appears at very shallow depths (<3 km).

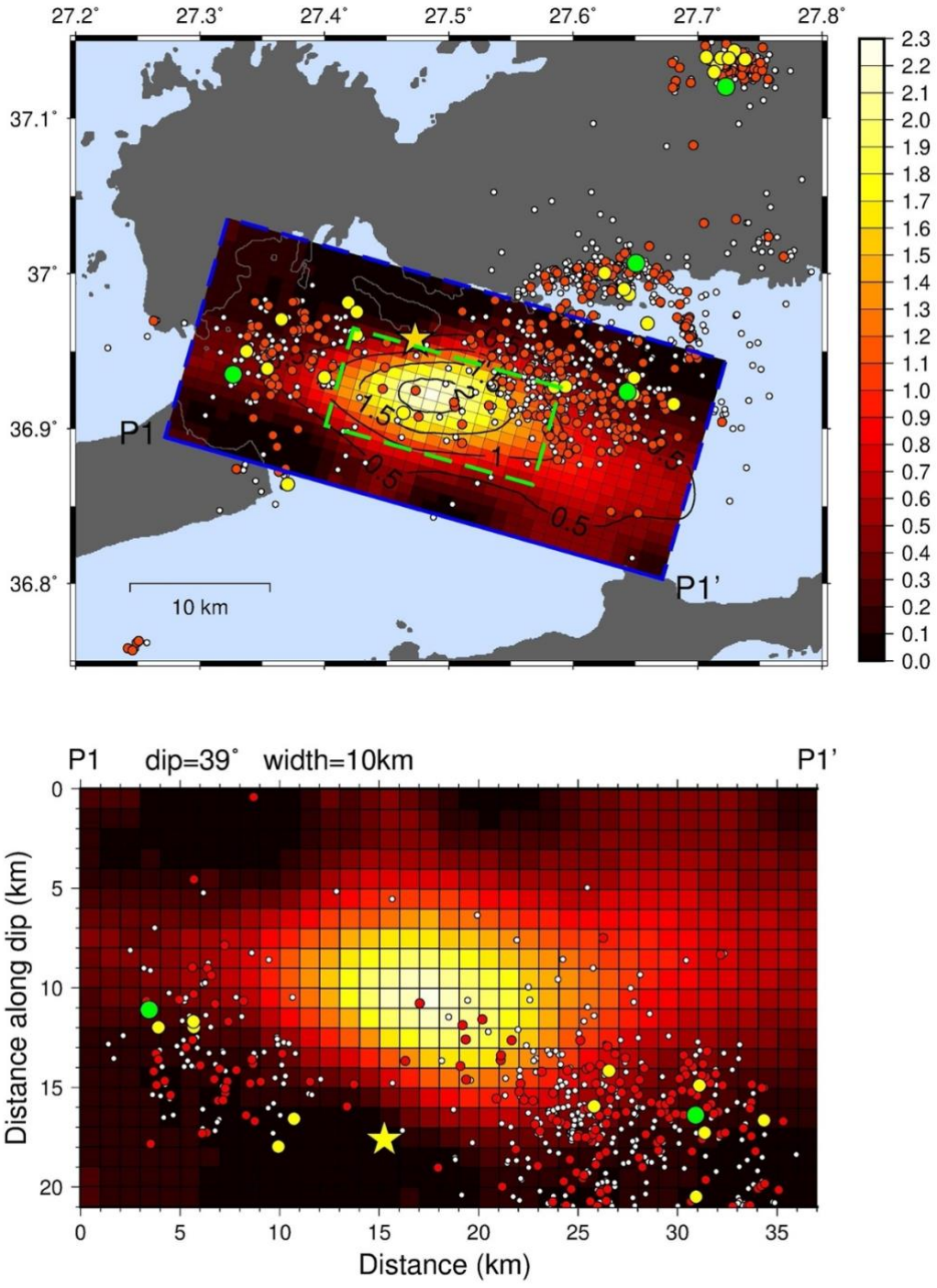

Figure 17. (a) Map projection of the variable slip distribution along with the relocated seismicity (Section 3). Slip values are in meters according to the color scale to the right. Green

dashed rectangle designates the fault geometry solution (Table 5) and blue dashed rectangle is the extended area used for the variable slip inversion. Dark isolines show contours for slips over 0.5 m with a 0.5 m step. **(b)** Strike parallel (P1-P1') cross section of the blue dashed rectangle along with the seismicity enclosed by the blue rectangle in (a)

For the modelling of the static surface displacements derived from the estimated slip distribution at the locations of the GNSS stations, we only considered the area of cells assigned a slip of 0.5 m or more as they constitute the main rupture area. The calculated model displacements at these positions are generally in agreement with the observed horizontal components (Fig. 18a, Table 4), while this is not the case for the observed vertical components where some of the stations are not adequately modelled (Fig. 18b – stations BODR, CAMK KNID, 086A). Discarding the higher uncertainties in GNSS vertical components (Table 4) as a possible result of additional subsidence due to soft sediments and their

compaction due to the vibration during the main shock, we consider that our model adequately represents the static displacement field.

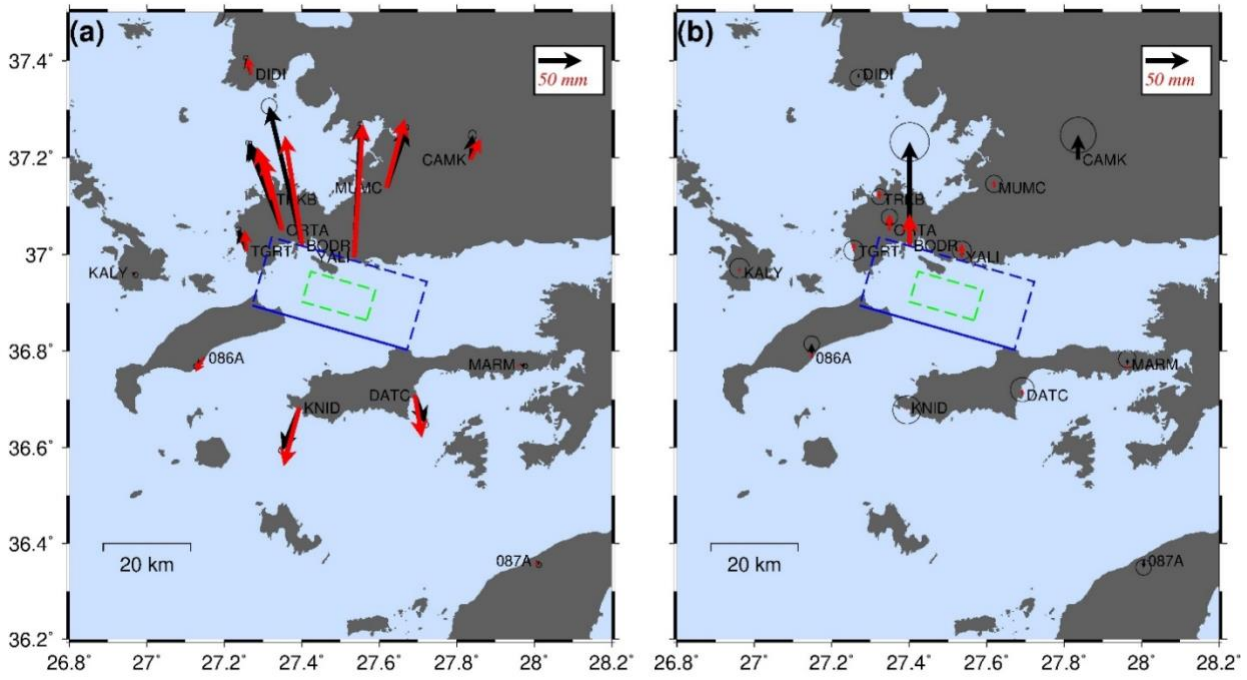

Figure 18. Displacement vectors – measured (black arrows) and modelled (red arrows), at the closest GNSS stations: **(a)** horizontal displacements, **(b)** vertical displacements. Blue and green dashed boxes are the same as in Figure 17.

6 Stress changes due to the main shock coseismic slip and possible triggering

Extensive research work has evidenced that strong earthquake occurrence either encourages or inhibits subsequent seismicity, depending upon its position and faulting properties relative to these of the main shock. The static stress changes provide the tool and are frequently used to explain the spatial aftershock distribution and its association with the stress field properties (King et al., 1994; Karakostas et al., 2003; Papadimitriou et al., 2017; among others). This is particularly the case in aftershock sequences, where the coseismic slip of the main shock triggers the occurrence of aftershocks, both onto and off the main fault. The stress transfer due to the main shock occurrence perturbs the local fault network. Thus, the aftershock activity is the result of stress residuals onto the main rupture (areas that did not slip during the main rupture) or stress increase beyond the fault edges due to stress

transfer. This also complies with the assumption that the main shock static stress changes in a given location favor the focal mechanisms aligned with the static stress change as well as the spatial distribution of seismicity in locations where the static stress change aligns with the background stress (Hardebeck, 2014).

Based on our detailed slip distribution model the Coulomb stress changes were estimated at three different depths. This has been done because the map view representation of the stress distribution pattern is considerably different at different depths, when the causative fault is not vertical or close to that geometry, but dips at a lower dip angle. Given the 39° dip angle of the main rupture, the multiple calculations of the stress pattern at different depths seems indispensable for its comparison with the aftershock locations.

For the coseismic stress changes calculation we followed the same approach as with the modelling of the slip at the position of the GNSS stations. More specifically, we considered cells with slip values of 0.5 m or more and treated each cell as a separate rectangular source with an area of 1x1 km^2, assuming a rigidity of 33GPa and a Poisson ratio of 0.25. Coulomb stress changes were calculated on three horizontal planes located in three different depths, namely 6 km, 9 km and 12 km, respectively (Fig. 19). In each case, the earthquakes with focal depths ±1.5 km above or beneath the calculation depth were plotted. Figure 19a shows the distribution of Coulomb stress changes calculated at the depth of 6 km. The magenta line is the inferred trace of the fault plane at that depth. The number of aftershocks is very limited in this depth range, with almost half of them beyond both fault edges, where the positive

stress changes have their highest values. Few aftershocks are located inside stress shadow areas.

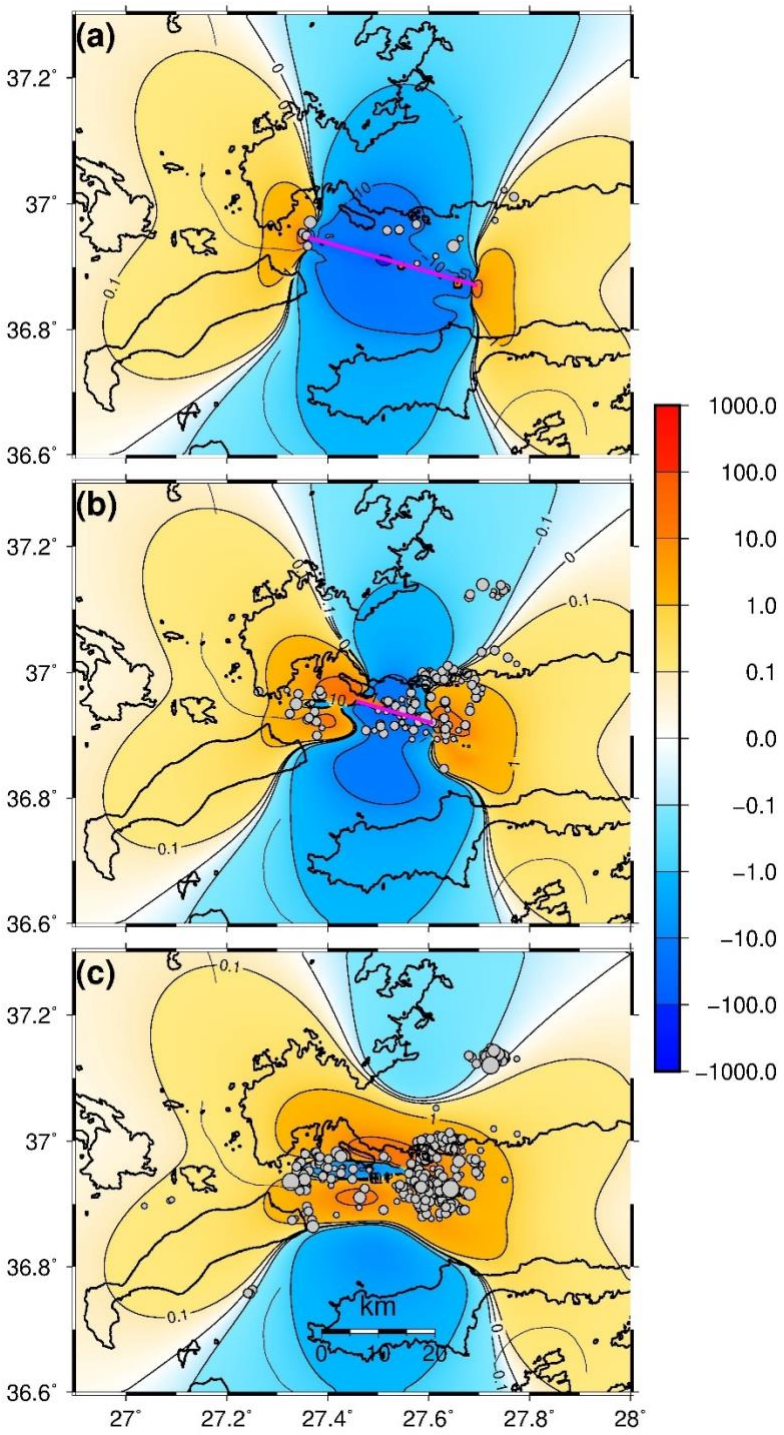

Figure 19. Coulomb stress changes caused from the variable coseismic slip model, calculated on three horizontal planes at depths of 6 km **(a)**, 9 km **(b)** and 12 km **(c)**, and given in bars

according to the color scale shown in the right hand side of the figure. Epicenters of the earthquakes are gray circles plotted in a crustal slice of ±1.5 km around that depth. Magenta lines denote the inferred fault trace in each depth for (a) and (b)

Figure 18b shows the distribution of Coulomb stress changes calculated at the depth of 9 km. The aftershock activity located in the depth range between 7.5 and 10.5 km is more intense than in the shallower depth range. Possible triggering is evidenced for a cluster located at the western fault tip, and the same can be stated for the largest percentage of the aftershock activity to the east of the eastern fault tip. Figure 18c shows the distribution of Coulomb stress changes at the depth of 12 km, below the lower part of the seismogenic fault. Almost all the seismic activity here collocates with stress-enhanced areas.

7 Discussion

The 2017 Kos aftershock sequence shares many similarities with previous sequences in the Aegean area, where multiple faults participated in the seismic excitation, with the secondary structures being triggered by the main rupture slip. The fault plane solutions and aftershock spatial distribution disclosed that the main shock nucleated at a structure that was favorably oriented with respect to the regional stress field and consequently failure of preexisting fault with optimal orientation. The latter is in turn part of the extensional complex network of active faults in the southeastern part of back arc Aegean area, where the intense stretching deformation attains the rate of 7 mm/yr (Nocquet, 2012). Strong (M>6.0) historical earthquakes are relatively rare in the study area, with a remarkable quiescence in the second half of the 20th century. Although moderate seismicity is not remarkable as well, in the period 2004-2011 eight earthquakes of M>5.0, took place near the main shock. The cumulative Coulomb stress changes caused from their coseismic slip, created a stress-enhanced area at the position of the 2017 main rupture.

The main shock triggered a vigorous aftershock sequence, which revealed secondary structures of the local fault network. Several hundreds of aftershocks followed, from which 1134 were relocated in this study, occurring in the next 103 days, mostly between 7 and 15 km, thus implying a crustal seismogenic layer with 8 km thickness and an unreformed upper crustal layer. The main shock produced clusters of off fault aftershocks, mainly occurred

beyond the eastern fault tip as well as one cluster of aftershocks occurred to the north, which raised concerns about possible triggering. This off fault activation was detected and investigated as involving stress transfer and triggering of closely spaced subparallel faults, which however is puzzling, as rupture on one fault segment may discourage on nearby potential slip interfaces. It is of interest to discuss that the coseismic slip amplitude varies with depth. It has been shown that the amount of slip in the middle of the seismogenic layer is systematically larger than the slip at larger or shallower depths, and negligible at the surface. This slip distribution agrees with the shear model for faults cutting through the velocity-strengthening layer in the top few kilometers of the crust (Scholz, 2019), where the coseismic slip is inhibited and most of slip occurs aseismically.

The proposed north dipping geometry, firstly suggested by Karakostas et al. (2018), supports the north dipping uniform slip fault proposed by Ganas et al. (2019) while the variable slip rupture shares common features with the north-dipping rupture models of Karasözen et al. (2018) and Konca et al. (2019), in terms of the extend of the rupture area, maximum slip depths and model geometry. The north dipping fault is further supported by tsunami simulations in both tide-gauge signals and water height distribution (Cordrie et al., 2021). The accurately located earthquakes along with the joint inversion for fault geometry led us to dismiss a south dipping fault plane. As it has been found, the maximum slip took place in the depth interval between 5 and 8 km, which perfectly agree with the pick of the depth distribution of the aftershocks. This in turn agrees with models that predict that the most favorable conditions for the earthquake nucleation are met at the mid depth of the seismogenic zone. Taking into account that the seismogenic layers in the Aegean area is in depths of 3-15 km, the results of our study suggest that the depth interval where instability dominates is at this part of the seismogenic layer. These findings are in full agreement with relevant results from recent seismic sequences in the Aegean area (e.g. Karakostas et al., 2021; Ganas et al., 2021). The positive Coulomb stress changes that were calculated with our

detailed slip model for the main shock are in satisfactory agreement between aftershock locations and stress changes comply with the stress triggering concept (e.g. King et al., 1994).

8 Conclusions

The results of aftershock analysis from the 2017 Kos main shock revealed that the combination of data from the seismological networks from both, Greece and Turkey, along with the relocation techniques and the analysis of the deformation field from DInSAR and the available GNSS displacement vectors contributed to achieve a more complete picture of the fault geometry and kinematics, and also to study the spatiotemporal evolution of the sequence. The improved double-difference depths in the cross sections clearly show a group of aftershocks consistent with the one of the nodal planes in the GCMT solution (and several more solutions that were determined in this study and adopted from other agencies), namely, the north-dipping one. The activated area exhibited a total lateral extent of about ~32 km. The aftershock focal depths range between 7-15 km, showing a peak concentration at 10-11 km. Focal mechanisms of aftershocks with moderate magnitudes also indicate a fault geometry consistent with the relocated seismicity and the focal mechanism of the main shock, and are consistent with the extensional regional stress pattern. The aftershock locations were not completely aligned with the strike of the main rupture, with abundant off fault seismicity.

A rupture model was built in a two-stage procedure, initially by joint inversion of seismological and geodetic data to infer fault geometry and then by inversion of geodetic data to derive a variable slip model. The proposed model is that of an asperity break with maximum slip values in depths between 5 and 8 km with significant slip values spreading to the eastern end of the fault, where the aftershock activity was more energetic. The largest portion of the coseismic slip occurred in one main patch down dip of the main rupture offshore, without extending to the shallow part and not reaching the surface. Our preferred model with the largest concentration of slip near the coastline and downdip under a submarine environment is in good agreement with the timing and magnitude of the observed tsunami and geological investigation for the observed displacement. It concerns a rather

simple rupture geometry where the maximum slip is concentrated onto a main patch of the rupture plane and the maximum slip occurred in the mid depth of the seismogenic layer.

Although there was an absence of strong earthquakes near the main shock area, several moderate (M4.7-5.5) earthquakes occurred from 2004-2011 in distances ranging between 15-30 km from the 2017 main shock epicenter. The calculation of the static stress field revealed that the 2017 main shock area lies in a stress-enhanced area increasing the likelihood of slip propagation in the area. The variable fault slip model, which was consequently used for calculating the Coulomb static stress changes induced by the main shock slip, contributed in deciphering that the spatial distribution of the aftershocks might be encouraged by stress transfer from the main rupture.

Acknowledgments

This research has been supported by the project “HELPOS–Hellenic System for Lithosphere Monitoring” (MIS 5002697) which is implemented under the Action “Reinforcement of the Research and Innovation Infrastructure”, funded by the Operational Programme "Competitiveness, Entrepreneurship and Innovation" (NSRF 2014–2020) and co–financed by Greece and the European Union (European Regional Development Fund). Geophysics Department Contribution 000. The study was also supported by the projects EPOS – European Plate Observing System (EPOS-PL) POIR.04.02.00-14-A003/16 and EPOS – European Plate Observing System (EPOS-PL+) POIR.04.02.00-00-C005/19-00, funded by the Operational Programme Smart Growth 2014-2020, Priority IV: Increasing the research potential, Action 4.2: Development of modern research infrastructure of the science sector and co-financed from European Regional Development Fund. The authors would like to express their gratitude to Witold Rohm and Jan Kapłon from the University of Environmental and Life Sciences, and Pavlos Bonatis from the Aristotle University of Thessaloniki, for the valuable discussions and comments on this study. Geophysics Department Contribution 000.

Open Research

The ΔCFS were computed with a program of J. Deng (Deng and Sykes, 1997), based on the DIS3D code of S. Dunbar (Erikson, 1986) and the expressions of G. Converse. The plots we

performed with the Generic Mapping Tools software (Wessel et al. 2013). For stations belonging to the HA, HL and HT networks data were collected from the NOA Node of EIDA (European Integrated Data Services – http://www.orfeus-eu.org/data/eida/) and for those belonging to the KO network from the KOERI node of EIDA (http://eida.koeri.boun.edu.tr/) and for those belonging to the AFAD network from the online database of AFAD (https://deprem.afad.gov.tr/). The Sentinel-1 data are freely available after account log-in at the Copernicus Sentinel Data, (2021). The Digital Elevation Model (DEM) used in the Sentinel-1 data processing is the freely available SRTM (EROS, doi:/10.5066/F7PR7TFT). The software used for the processing of the Sentinel-1 data is Sentinel Application Platform (SNAP,). The correction for atmospheric delays applied to the Sentinel-1 data is Generic Atmospheric Correction Online Service (GACOS, Yu et al., 2017). The GNSS data are retrived from the scientific publications Ganas et al. (2019) and Tiryakioglu et al. (2018). The data integration and source modelling (section 4 and 5) are perfomed using various software tools under the Pyrocko toolbox (Heimann et al., 2017).

References

AFAD, Disaster and Emergency Management Authority (1990). Republic of Turkey Prime Ministry, Disaster & Emergency Management Authority, Presidential of Earthquake Department [data set]. International Federation of Digital Seismograph Networks https://doi.org/10.7914/SN/TU

Akyol, N., Zhu, L., Mitchell, B. J., Sözbilir, H. & Kekovalı, K. (2006). Crustal structure and local seismicity in western Anatolia. *Geophysical Journal International*, 166(3), 1259-1269, https://doi.org/10.1111/j.1365-246X.2006.03053.x

AUTH, Aristotle University of Thessaloniki (1981). Aristotle University of Thessaloniki Seismological Network [Data set]. *International Federation of Digital Seismograph Networks*, https://doi.org/10.7914/SN/HT

Chen, C.W. & Zebker, H.A. (2000). Network approaches to two-dimensional phase unwrapping: Intractability and two new algorithms. *Journal of the Optical Society of America A*, 17(3), 401-414, https://doi.org/10.1364/JOSAA.17.000401

828 Copernicus Sentinel Data (2021). European Space Agency, https://scihub.copernicus.eu/

829 Cordrie, L., Gailler, A., Heinrich, P., Briole, P. & Ganas, A. (2021). The July 20, 2017 Mw = 6.6
830 Bodrum-Kos Earthquake, Southeast Aegean Sea: Contribution of the Tsunami Modeling to
831 the Assessment of the Fault Parameters. *Pure and Applied Geophysics*,
832 https://doi.org/10.1007/s00024-021-02766-3

833 Daout, S., Steinberg, A., Isken, M.P., Heimann, S. & Sudhaus, H. (2020). Illuminating the spatio-
834 temporal evolution of the 2008-2009 Qaidam earthquake sequence with the joint use of
835 InSAR time series and teleseismic data. *Remote Sensing*, 12(17), 2850,
836 https://doi.org/10.3390/rs12172850

837 Deng, J. & Sykes, L. (1997). Evolution of the stress field in Southern California and triggering
838 of moderate size earthquakes: A 200–year perspective. *Journal of Geophysical Research: Solid*
839 *Earth*, 102(B5), 9859-9886, https://doi.org/10.1029/96JB03897

840 Dogru, F. (2020). The Importance of Atmospheric Corrections on InSAR Surveys Over
841 Turkey: Case Study of Tectonic Deformation of Bodrum-Kos Earthquake. *Pure and Applied*
842 *Geophysics*, 177, 5761–5780, https://doi.org/10.1007/s00024-020-02606-w

843 Efron, B. (1982). The Jackknife, the Bootstrap and other resampling plans. *CBMS-NSF*
844 *Regional Conference Series in Applied Mathematics*, Series Number 38, 5-11, ISBN: 978-0-
845 89871-179-0, https://doi.org/10.1137/1.9781611970319

846 Earth Resources Observation and Science (EROS) Center. (2017). Shuttle Radar Topography
847 Mission (SRTM) 1 Arc-Second Global [Data set]. *U.S. Geological Survey*,
848 https://doi.org/10.5066/F7PR7TFT

849 Erickson, L. (1986). *User's manual for DIS3D: A three-dimensional dislocation program with*
850 *applications to faulting in the Earth*. Master's Thesis, Stanford University. Department of
851 Applied Earth Sciences, pp.167

852 Foumelis, M., Papazachos, C., Papadimitriou, E., Karakostas, V., Ampatzidis, D., Moschopoulos,
853 G. et al. (2021). On rapid multidisciplinary response aspects for Samos 2020 M7.0

854 earthquake. *Acta Geophysica*, 69, 1025–1048, https://doi.org/10.1007/s11600-021-00578-
855 6

856 Ganas, A., Elias, P., Kapetanidis, V., Valkaniotis, S., Briole, P., Kassaras, I et al. (2019).The July
857 20, 2017 M6.6 Kos Earthquake: Seismic and Geodetic Evidence for an Active North-Dipping
858 Normal Fault at the Western End of the Gulf of Gökova (SE Aegean Sea). *Pure and Applied*
859 *Geophysics*, 176, 4177–4211, https://doi.org/10.1007/s00024-019-02154-y

860 Ganas, A., Elias, P., Briole, P., Valkaniotis, S., Escartin, J., Tsironi, V., Karasante, I. & Kosma, C.
861 (2021). Co-seismic and post-seismic deformation, filed observations and fault model of the
862 30 October 2020 Mw7.0 Samos earthquake, Aegean Sea. *Acta Geophysica*, 69, 999-1024,
863 https://doi.org/10.1007/s11600-021-00599-1

864 Goldstein, R. M. & Werner, C. L. (1998). Radar interferogram filtering for geophysical
865 applications. *Geophysical Journal International*, 25(21), 4035-4038,
866 https://doi.org/10.1029/1998GL900033

867 Hanks, T.C. & Kanamori, H. (1979). A moment magnitude scale. *Journal of Geophysical*
868 *Research*, 84(B5), 2348-2350, https://doi.org/10.1029/JB084iB05p02348

869 Hardebeck, J. L. (2014). The impact of static stress change, dynamic stress change, and the
870 background stress on aftershock focal mechanisms. *Journal of Geophysical Research: Solid*
871 *Earth*, 119(11), 8239-8266, https://doi.org/10.1002/2014JB011533

872 Heiderzaden, M., Necmioglu, O., Ishibe, T. & Yalciner, A. (2017). Bodrum–Kos (Turkey–
873 Greece) Mw6.6 earthquake and tsunami of 20 July 2017: a test for the Mediterranean
874 tsunami warning system. *Geoscience Letters*, 4 (31), 1-11, https://doi.org/10.1186/s40562-
875 017-0097-0

876 Heimann, S., Kriegerowski, M., Isken, M., Cesca, S., Daout, S., Grigoli, F., et al. (2017). *Pyrocko*
877 *– An open-source seismology toolbox and library*. V. 0.3. GFZ Data Services.
878 https://doi.org/10.5880/GFZ.2.1.2017.001

879 Heimann, S., Isken, M., Kühn, D., Sudhaus, H., Steinberg, A., Daout, S., Cesca, S., Vasyura-
880 Bathke, H., Dahm, T. (2018). *Grond – A probabilistic earthquake source inversion framework*.
881 V. 1.0. GFZ Data Services. https://doi.org/10.5880/GFZ.2.1.2018.003

882 HUSN, National Observatory of Athens, Institute of Geodynamics, Athens. (1975). National
883 Observatory of Athens Seismic Network [Data set]. *International Federation of Digital*
884 *Seismograph Networks*, https://doi.org/10.7914/SN/HL

885 Isken, M., Sudhaus, H., Heimann, S., Steinberg, A., Daout, S. & Vasyura-Bathke, H. (2017). *Kite*
886 *– Software for Rapid Earthquake Source Optimisation from InSAR Surface Displacement*. V. 0.1.
887 GFZ Data Services. https://doi.org/10.5880/GFZ.2.1.2017.002

888 Jónsson, S., Zebker, H.A., Segall, P. & Amelung, F. (2002). Fault slip distribution of the 1999
889 Mw7.2 Hector Mine earthquake, California, estimated from satellite radar and GPS
890 measurements. *Bulletin of the Seismological Society of America*, 92(4), 1377–1389,
891 http://dx.doi.org/10.1785/0120030038

892 Karakostas, V.G., Papadimitriou, E.E., Karakaisis, G.F., Papazachos, C.B., Scordilis, E.M.,
893 Vargemezis, G., & Aidona, E. (2003). The 2001 Skyros, Northern Aegean, Greece, earthquake
894 sequence: off-fault aftershocks, tectonic implications, and seismicity triggering. *Geophysical*
895 *Research Letters*, 30(1), 12-1-12-4, https://doi.org/10.1029/2002GL015814

896 Karakostas, V.G., Papadimitriou, E.E., Mesimeri, M. & Civgin, B. (2018). The 2017 Kos
897 sequence: aftershocks relocation and implications for activated fault segments. *Book of*
898 *Abstracts of the 36th General Assembly of the European Seismological Commission*, Valetta,
899 Malta, 2-7 September 2018, ESC2018-S6-645, ISBN: 978-88-98161-12-6

900 Karakostas, V., Tan, O., Kostoglou, A., Papadimitriou, E. & Bonatis, P. (2021). Seismotectonic
901 implications of the 2020 Samos, Greece, Mw7.0 main shock based on high–relocation and
902 source slip model. *Acta Geophysica*, 69, 979-996, https://doi.org/10.1007/s11600-021-
903 00580-y

904 Karasözen, E., Nissen, E., Büyükakpınar, P., Cambaz, M.D., Kahraman, M., Ertan, E. K., et al.
905 (2018). The 2017 July 20 Mw6.6 Bodrum-Kos earthquake illuminates active faulting in the

906 Gulf of Gokova, SW Turkey. *Geophysical Journal International*, 214(1), 185-199,
907 https://doi.org/10.1093/gji/ggy114

908 King, G. C. P., Stein, R. S. & Lin, J. (1994). Static stress changes and the triggering of
909 earthquakes. *Bulletin of the Seismological Society of America*, 84(3), 935-953,
910 https://doi.org/10.1785/BSSA0840030935

911 Kiratzi, A. & Koskosidi, A. (2018). *Constraints on the near–source motions of the Kos–Bodrum*
912 *20 July 2017 Mw6.6 earthquake*. Paper presented at 16th European Conference on
913 Earthquake Engineering, Thessaloniki, Greece, 18-21 June 2018

914 Klein, F. W. (2002). User's Guide to HYPOINVERSE–2000, a Fortran program to solve
915 earthquake locations and magnitudes (Open-File Report 2002-171). *U.S. Geological Survey*,
916 https://doi.org/10.3133/ofr02171

917 KOERI, Kandilli Observatory and Earthquake Research Institute, Boğaziçi University (1971).
918 Bogazici University Kandilli Observatory and Earthquake Research Institute [Data set].
919 *International Federation of Digital Seismograph Networks*, https://doi.org/10.7914/SN/KO

920 Konca, A. O., Guvercin, S. E., Ozarpaci, S., Ozdemir, A., Funning, G. J., Dogan, U., et al (2019).
921 Slip distribution of the 2017 Mw6.6 Bodrum-Kos earthquake: resolving the ambiguity of
922 fault geometry. *Geophysical Journal International*, 219(2), 911-923,
923 https://doi.org/10.1093/gji/ggz332

924 Kurt, H., Demirbağ, E. & Kuşçu, İ. (1999). Investigation of the submarine active tectonism in
925 the Gulf of Gökova, southwest Anatolia-southeast Aegean Sea, by multi–channel seismic
926 reflection data. *Tectonophysics*, 305(4), 477-496, https://doi.org/10.1016/S0040-
927 1951(99)00037-2

928 Massonnet, D., Rossi, M., Carmona, C., Adragna, F., Peltzer, G., Feigl, K. & Rabaute, T. (1993).
929 The displacement field of the Landers earthquake mapped by radar interferometry. *Nature*,
930 364, 138-142, https://doi.org/10.1038/364138a0

McClusky, S., Balassanian, S., Barka, A., Demir, C., Ergintav, S., Georgiev, I., et al. (2000). Global Positioning System constraints on plate kinematics and dynamics in the eastern Mediterranean and Caucasus. *Journal of Geophysical Research*, 105 (B3), 5695-5719, https://doi.org/10.1029/1999JB900351

Nocquet, J.-M. (2012). Present-day kinematics of the Mediterranean: a comprehensive overview of GPS results. *Tectonophysics*, 579, 220-242, https://doi.org/10.1016/j.tecto.2012.03.037

Ocakoğlu, N., Nomikou, P., İşcan, Y., Loreto, M. F. & Lampridou, D. (2018). Evidence of extensional and strike-slip deformation in the offshore Gökova-Kos area affected by the July 2017 Mw6.6 Bodrum-Kos earthquake, eastern Aegean Sea. *Geo-Marine Letters*, 38, 211-225. https://doi.org/10.1007/s00367-017-0532-4

Okada, Y. (1992). Internal deformation due to shear and tensile faults in a half-space. *Bulletin of the Seismological Society of America*, 82(2), 1018-1040, https://doi.org/10.1785/BSSA0820021018

Papadimitriou, E. E. (2002). Mode of strong earthquake occurrence in central Ionian Islands (Greece). Possible triggering due to Coulomb stress changes generated by the occurrence of previous strong shocks. *Bulletin of the Seismological Society of America*, 92(8), 3293-3308, https://doi.org/10.1785/0120000290

Papadimitriou, E., Sourlas, G. & Karakostas, V. (2005). Seismicity variations in the Southern Aegean, Greece, before and after the large (M7.7) 1956 Amorgos earthquake due to evolving stress. *Pure and Applied Geophysics*, 162, 783-804. https://doi.org/10.1007/s00024-004-2641-z

Papadimitriou, E., Karakostas, V., Mesimeri, M., Chouliaras, G. & Kourouklas, Ch. (2017). The Mw6.7 17 November 2015 Lefkada (Greece) earthquake: structural interpretation by means of aftershock analysis. *Pure and Applied Geophysics*, 174, 3869-3888, https://doi.org/10.1007/s00024-017-1601-3

957 Papazachos, B.C. & Papazachou, C. C. (2003). The earthquakes of Greece. *Ziti Publication Co.,*
958 *Thessaloniki, Greece*, pp. 304 (in Greek)

959 Papazachos, B.C., Papadimitriou, E. E., Kiratzi, A. A., Papazachos, C. B., & Louvari, E. K. (1998).
960 Fault plane solutions in the Aegean sea and the surrounding area and their tectonic
961 implication. *Bollettino Di Geofisica Teorica Ed Applicata*, 39, 199-218

962 Papazachos, B., Scordilis, E., Panagiotopoulos, D., Papazachos, C., & Karakaisis, G. (2004).
963 Global relations between seismic fault parameters and moment magnitude of earthquakes.
964 *Bulletin of the Geological Society of Greece*, 36(3), 1482-1489,
965 https://doi.org/10.12681/bgsg.16538

966 Pondrelli, S., Salimbeni, S., Morelli, A., Ekström, G. & Boschi, E. (2007). European-
967 Mediterranean Regional Centroid Moment Tensor catalog: Solutions for years 2003 and
968 2004. *Physics of the Earth and Planetary Interiors*, 164(1-2), 90-112,
969 https://doi.org/10.1016/j.pepi.2007.05.004

970 Pondrelli, S., Salimbeni, S., Morelli, A., Ekström, G., Postpischl, L., Vannucci, G. & Boschi, E.
971 (2011). European–Mediterranean Regional Centroid Moment Tensor catalog: Solutions for
972 2005-2008. *Physics of the Earth and Planetary Interiors*, 185(3-4), 74-81,
973 https://doi.org/10.1016/j.pepi.2011.01.007

974 Reilinger, R., McClusky, S., Paradissis, D., Ergintav, S. & Vernant, P. (2010). Geodetic
975 constraints on the tectonic evolution of the Aegean region and strain accumulation along the
976 Hellenic subduction zone. *Tectonophysics*, 488(1-4), 22-30,
977 https://doi.org/10.1016/j.tecto.2009.05.027

978 Sboras, S., Lazos, S., Mouzakiotis, E., Karastathis, V., Pavlides, S. & Chatzipetros, A. (2020).
979 Fault modelling, seismic sequence evolution and stress transfer scenarios for the July 20,
980 2017 (Mw6.6) Kos-Gokova Gulf earthquake, SE Aegean. *Acta Geophysica*, 68, 1245-1261,
981 https://doi.org/10.1007/s11600-020-00471-8

982 Schaff, D. P. & Beroza, G. C. (2004). Coseismic and postseismic velocity changes measured by
983 repeating earthquakes. *Journal of Geophysical Research*, 109(B10),
984 https://doi.org/10.1029/2004JB003011

985 Schaff, D. P. & Waldhauser, F. (2005). Waveform cross-correlation-based differential travel-
986 time measurements at the northern California seismic network. *Bulletin of the Seismological*
987 *Society of America*, 95(6), 2446-2461, https://doi.org/10.1785/0120040221

988 Scholz, C. H. (2019). *The mechanics of earthquakes and faulting*. Cambridge University Press,
989 New York, 3rd edition, pp. 517, ISBN: 9781316681473,
990 https://doi.org/10.1017/9781316681473

991 SNAP, ESA Sentinel Application Platform v8.0.0, http://step.esa.int

992 Sokos, E. & J. Zahradnik, (2008). ISOLA a Fortran code and a Matlab GUI to perform multiple-
993 point source inversion of seismic data. *Computers & Geosciences*, 34(8), 967-977,
994 https://doi.org/10.1016/j.cageo.2007.07.005

995 Sokos, E. & J. Zahradník (2013). Evaluating Centroid-Moment-Tensor Uncertainty in the New
996 Version of ISOLA Software. *Seismological Research Letters*, 84(4), 656-665.
997 https://doi.org/10.1785/0220130002

998 Tiryakioğlu, İ, Aktuğ, B., Yiğit, C. Ö., Yavaşoğlu, H. H., Sözbilir, H., Özkaymak, Ç, et al. (2018).
999 Slip distribution and source parameters of the 20 July 2017 Bodrum-Kos earthquake
1000 (Mw6.6) from GPS observations. *Geodinamica Acta*, 30(1), 1-14,
1001 https://doi.org/10.1080/09853111.2017.1408264

1002 Tur, H., Yaltırak, C., Elitez, I. & Sarıkavak, K. T. (2015). Pliocene–Quaternary tectonic
1003 evolution of the Gulf of Gökova, southwest Turkey. *Tectonophysics*, 638, 158–176,
1004 https://doi.org/10.1016/j.tecto.2014.11.008

1005 Uluğ, A., Duman, M., Ersoy, Ş., Özel, E. & Avcı, M. (2005). Late Quaternary sea-level change,
1006 sedimentation and neotectonics of the Gulf of Gökova: Southeastern Aegean Sea. *Marine*
1007 *Geology*, 221, 381-95, https://doi.org/10.1016/j.margeo.2005.03.002

1008 Vasyura-Bathke, H., Dettmer, J., Steinberg, A., Heimann, S., Isken, M., Zielke, O., et al (2019).
1009 *BEAT – Bayesian Earthquake Analysis Tool*. V. 1.0. GFZ Data Services.
1010 https://doi.org/10.5880/fidgeo.2019.024

1011 Vasyura-Bathke, H., Dettmer, J., Steinberg, A., Heimann, S., Isken, M.P., Zielke, O., et al (2020).
1012 The Bayesian Earthquake Analysis Tool. *Seismological Research Letters*, 91(2A), 1003–1018,
1013 https://doi.org/10.1785/0220190075

1014 Wadati, K. & Oki., S. (1933). On the travel time of earthquake waves (Part II). *Journal of the*
1015 *Meteorological Society of Japan,* Ser. II, 1933, Volume 11, Issue 1, Pages 14-28,
1016 https://doi.org/10.2151/jmsj1923.11.1_14

1017 Waldhauser, F. (2001). HypoDD-a program to compute double-difference hypocenter
1018 locations (Open-File Report 2001-113). *U.S. Geological Survey*, pp. 01-113,
1019 https://doi.org/10.3133/ofr01113

1020 Waldhauser, F. & Ellsworth, W. L. (2000). A double-difference earthquake location
1021 algorithm: method and application to the northern Hayward fault, California. *Bulletin of the*
1022 *Seismological Society of America*, 90(6), 1353–1368, https://doi.org/10.1785/0120000006

1023 Wang, R. (1999): A simple orthonormalization method for the stable and efficient
1024 computation of Green's functions. *Bulletin of the Seismological Society of America*, 89(3), 733-
1025 741, https://doi.org/10.1785/BSSA0890030733

1026 Wang, R., Lorenzo-Martín, F. & Roth, F. (2006). PSGRN/PSCMP – a new code for calculating
1027 co- and post–seismic deformation, geoid and gravity changes based on the viscoelastic-
1028 gravitational dislocation theory. *Computers & Geosciences*, 32(4), 527–541,
1029 https://doi.org/10.1016/j.cageo.2005.08.006

1030 Wells, D. L. & Coppersmith, K. J. (1994). New empirical relationships among magnitude,
1031 rupture length, rupture width, rupture area, and surface displacement. *Bulletin of the*
1032 *Seismological Society of America*, 84(4), 974-1002,
1033 https://doi.org/10.1785/BSSA0840040974

1034 Wessel, P., Smith, W.H.F., Scharroo, R., Luis, J. & Wobbe, F. (2013). Generic Mapping Tools:
1035 Improved Version Released. *EOS, Transactions American Geophysical Union*, 94(45), 409-
1036 410, https://doi.org/10.1002/2013EO450001

1037 Wiemer, S. & Wyss, M. (2000). Minimum magnitude of completeness in earthquake catalogs:
1038 Examples from Alaska, the Western United States, and Japan. *Bulletin of the Seismological*
1039 *Society of America*, 90(4), 859–869, https://doi.org/10.1785/0119990114

1040 Yolsal-Çevikbilen, S., Taymaz, T. & Helvacı, C. (2014). Earthquake mechanisms in the Gulfs of
1041 Gökova, Sığacık, Kuşadası, and the Simav Region (western Turkey): Neotectonics,
1042 seismotectonics and geodynamic implications. *Tectonophysics*, 635, 100-124,
1043 https://doi.org/10.1016/j.tecto.2014.05.001

1044 Yu, C., Penna, N. T. & Li, Z. (2017). Generation of real-time mode high-resolution water vapor
1045 fields from GPS observations. *Journal of Geophysical Research: Atmosphere*, 122(3), 2008–
1046 2025, https://doi.org/10.1002/2016JD025753